# We are IntechOpen, the world's leading publisher of Open Access books
# Built by scientists, for scientists

## 4,800
Open access books available

## 122,000
International authors and editors

## 135M
Downloads

## 154
Countries delivered to

Our authors are among the

## TOP 1%
most cited scientists

## 12.2%
Contributors from top 500 universities

**WEB OF SCIENCE**™

Selection of our books indexed in the Book Citation Index
in Web of Science™ Core Collection (BKCI)

# Interested in publishing with us?
# Contact book.department@intechopen.com

Numbers displayed above are based on latest data collected.
For more information visit www.intechopen.com

# A Technique for Time-Resolved Imaging of Millimeter Waves Based on Visible Continuum Radiation from a Cs-Xe DC Discharge — Fundamentals and Applications

Mikhail S. Gitlin

## Abstract

The chapter presents a review of a highly sensitive technique for time-resolved imaging and measurement of the 2D intensity profiles of millimeter waves (MMW) based on the use of visible continuum radiation (VCR) from the positive column (PC) of a medium pressure Cs-Xe DC discharge (VCRD technique). The review focuses on the operating principles, fundamentals, and applications of this new technique. The design of a discharge tube and an experimental setup which were used to create a wide homogeneous PC plasma slab are described. The MMW effects on the plasma slab are studied. The mechanism of microwave-induced variations in the VCR intensity and the causes of violation of the local relation between the visible continuum emissivity and the MMW intensity are discussed. The main characteristics, e.g., spatial and temporal resolution, and sensitivity of the VCRD technique have been evaluated. Experiments on imaging of the field patterns of horn antennas and quasioptical beams demonstrated that the VCRD technique can be used for a good-quality imaging of the MMW beams in the entire MM-wavelength band. The VCRD technique was applied for imaging of output field patterns of the MMW electron tubes and determination of some of their characteristics, as well as for active real-time imaging and nondestructive testing using MM waves.

**Keywords:** Microwaves, Imaging, Electric discharges, Continuum

## 1. Introduction

Millimeter waves (MMWs) are electromagnetic (EM) waves with wavelengths ranging from 1 to 10 mm in free space. Millimeter waves are widely used in radar, navigation, telecommunications, remote sensing, plasma heating and diagnostics, material processing, spectroscopy, etc. Imaging and nondestructive testing (NDT) with millimeter waves is also of great interest

for scientific, industrial, security, and biomedical applications [1–10]. In many MMW applications, as well as for engineering of MMW devices and systems, it is necessary to measure the spatial profiles of MMW radiation in real time. Electronic, electro-optic (EO), and thermographic techniques are commonly used for measuring and imaging the MMW field profiles. The electronic techniques employ receivers with semiconductor [4–9], superconducting [10], and glow discharge [11–13] MMW detectors. Electro-optic techniques use EO sensors for MM waves [14, 15]. Mechanically scanned receiver systems are widespread. However, a mechanically scanned receiver cannot be applied for a time-resolved imaging of MMW field profiles. Time-resolved images of MMW beams can be obtained with two-dimensional (2D) antenna arrays with MMW detectors [4–8, 12, 13]. The images of MMW beams obtained using 2D antenna arrays are of rather poor quality, because of the element-to-element gain and sensitivity variations, large element-to-element spacing, and small number of sensor elements. Because of the strong scattering and reflection of millimeter waves from antenna arrays, they can hardly be used for near-field imaging. Moreover, 2D antenna arrays are expensive and sophisticated systems. A live electro-optic camera has recently been used for imaging of traveling millimeter waves at video frame rates [15]. However, a live 2D electro-optic imaging system is a very complex system as well. Small aperture of the modern live EO sensor is another disadvantage of this technique. In thermographic techniques of measuring of the MMW beam profiles, thermo-sensitive phosphor or liquid crystal films, thermal paper, and dielectric sheets are used as screens, which are irradiated with millimeter waves. Thermographic techniques, which use thermo-sensitive phosphor [16, 17] or liquid crystal films [18], provide images of MMW intensity profiles in the visible region. A very simple way of obtaining MMW beam images in the visible region is based on the utilization of thermal papers. However, only rough time-integrated images of the field profiles of high-energy MMW beams can be obtained by using thermal paper [19]. In another variant of the thermographic technique, a flat sheet of dielectric material (e.g., paper, polyvinylchloride) is used as an absorbing screen for MMWs [20–23]. A spatial distribution of the microwave-induced variation in the screen temperature is measured by an infrared (IR) camera. This technique has proven itself well in installation, adjustment, and evaluation of the characteristics of the MMW transmission lines and sources of CW and long-pulse high-power millimeter waves. The main drawbacks of all thermographic methods of the MMW imaging are their low temporal resolution, which can be 10 ms at best, and low energy flux sensitivity, which is no better than 1 mJ/cm$^2$. Moreover, distortions, which are caused by heat conduction, can significantly impair the quality of thermographic images of MMW beams. These distortions increase with increasing MMW pulse duration or camera exposure time.

Light emission from microwave-induced gas breakdowns in space and in gas-filled tubes (luminescent lamps, neon indicator lamps, etc.), as well as breakdowns near a dielectric surface coated with a thin layer of metal powder, have been exploited to analyze the field profiles of millimeter waves [24, 25]. However, the microwave-induced breakdown yields rough distorted images of the field pattern of high-power pulsed MM waves. This technique operates only for narrow ranges of MMW intensities and pulse durations. It is impossible to obtain good-quality images by using this technique because of the properties both of the microwave-breakdown plasma and the light emission from such a plasma. No plasma glow is observed

when the intensity of millimeter waves is below the breakdown threshold, or the MMW pulse duration is shorter than the time to breakdown. When the breakdown threshold is exceeded, a filamentary array with subwavelength spacing is formed in space if a gas pressure is higher than a few Torr [26]. The electron density in the filaments is higher than the critical plasma density; therefore, millimeter waves are reflected and scattered by the filaments. The boundary of the region occupied by the breakdown plasma propagates towards the MMW beam. The main contribution to the light emission from the breakdown plasma is given by a bound-bound transition between electronic levels of atoms and molecules. The dependences of the intensity of the atomic and molecular emission lines on the MMW intensity are sophisticated and nonlinear. Moreover, the dependences are different for different spectral lines.

The above-specified drawbacks of the conventional techniques for imaging and measurement of the MMW field profiles require their further improvement, as well as the development of alternative techniques. Recently, a technique for imaging of MMWs based on visible continuum (VC) radiation from a slab of the positive column (PC) of a medium-pressure DC discharge in a mixture of cesium vapor and xenon (a Cs-Xe DC discharge) was proposed and developed [27–35]. The idea behind this MMW imaging technique is to use the effect of the increase in intensity of the VC radiation from the PC of a Cs-Xe discharge due to MMW electron heating. By means of this technique, MMW beam profiles are converted into visible images, thus allowing a conventional digital camera with an optical filter to acquire the images. This review is focused on the operating principles, fundamentals, and applications of this new technique for imaging of MMWs. The chapter is organized as follows. Section 2 provides methods for a plasma slab generation using a Cs-Xe DC discharge and its diagnostics. Section 3 focuses on the experimental evaluation of some important characteristics of the technique for MMW imaging, which is based on using visible continuum radiation from the discharge (VCRD) in a mixture of Cs-Xe. We shall call this technique for imaging of MMWs a VCRD technique. In Section 3, experiments on imaging of the field profiles at the output of MMW horn antennas and quasioptical MMW beams are also discussed. The subjects of Section 4 are the fundamentals of the VCRD technique for imaging of MMWs. In particular, it discusses the nature of the visible continuum radiation (VCR) from the PC of a Cs-Xe discharge, the mechanism of microwave-induced variations in the VCR intensity, and the causes of violation of the local relation between the VC emissivity and the MMW intensity. Section 5 reviews applications of the VCRD technique for imaging of output field patterns of short-wavelength MMW vacuum electron tubes and determination of some characteristics of these tubes. Applications of the VCRD technique for real-time imaging and nondestructive testing using MMWs are also the subject of Section 5.

## 2. Plasma slab generation using a Cs-Xe DC discharge and experimental study of its characteristics

A sealed discharge tube (DT) was used to generate a slab of the positive column of a Cs-Xe DC discharge in the experiments on imaging of MM waves [27]. Figures 1(a) and 1(b) show side and top views of the discharge tube. A hollow rectangular parallelepiped was located at the

center of the tube. It was glued from fused quartz plates. Two square quartz windows with 10 × 10 cm² apertures and 0.65 cm thick were set at a distance of 2 cm from each other. They were used to form the plasma slab and input the MMW beam into the discharge tube. Two plane anodes and two heated cathodes were sealed in glass cylinders 10 cm in diameter. The glass cylinders were glued to the quartz cell. The distance between the anodes and cathodes was 30 cm. Each pair of electrodes was powered by a separate power supply. Two pairs of thin quartz plates with a size of 5 × 9 cm² were installed inside the cylinders parallel to each other at a distance of 2 cm. These two pairs of quartz plates restricted the region in the cylinders occupied by the positive column and increased the length of a homogeneous part of the PC plasma. The longitudinal electric field $E$ in the positive column was determined using the difference in potentials between the electrical probes. The discharge tube was filled with 45 Torr xenon. The tube had side arms in which drops of cesium metal were placed. Cesium was a readily ionized seed. To obtain the required density of cesium vapor, the discharge tube was heated by a hot air flow in an oven (see Figure 1(c)). The DT wall temperature was measured using thermocouples. The oven has one or two quartz windows 20 cm in diameter. The spectrum of visible radiation emitted by the PC of a Cs-Xe discharge was recorded by a monochromator (see Figure 1(c)). A lens focused light from the PC onto the input slit of the monochromator. A photomultiplier tube was attached to the exit slit of the monochromator. A signal from the photomultiplier was recorded by a digital oscilloscope. The data from the oscilloscope were saved to a computer and processed. The relative calibration of the spectroscopic system in a spectral region from 350 to 700 nm was performed with a tungsten ribbon lamp.
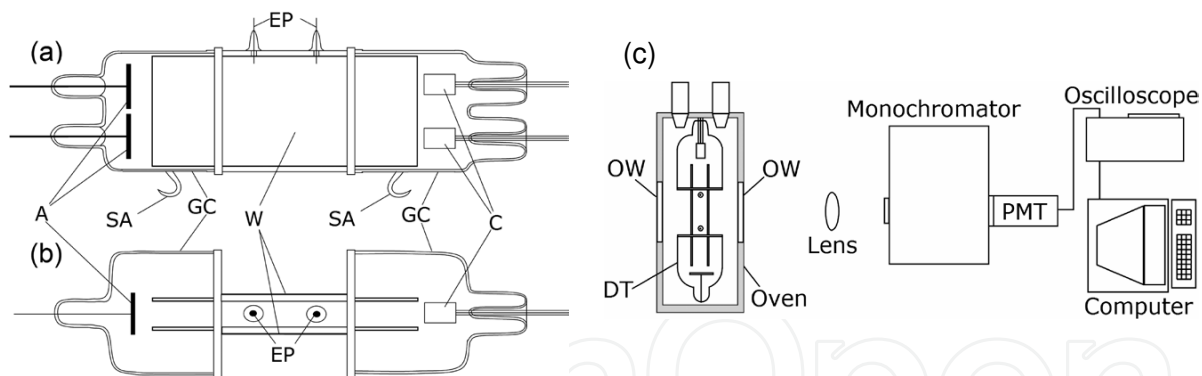


**Figure 1.** (a) Side and (b) top views of the discharge tube used to generate a slab of the positive column of a Cs-Xe DC discharge; A: anodes; C: cathodes; W: quartz windows; GC: glass cylinder; SA: sidearm; EP: electrical probes. (c) Schematic diagram of the experimental setup (top view) used for a study of emission spectra of light from the PC of a Cs-Xe discharge; DT: discharge tube; OW: oven window; PMT: photomultiplier tube.

The characteristics of the positive column of a Cs-Xe discharge and the spectrum of the light from the PC plasma were studied when there were no incident MM waves [27, 28]. The discharge current $J$ was 1.5 A and the DT wall temperature varied from 80°C to 120°C, which corresponded to the partial pressures of Cs vapor from about $10^{-4}$ to $2 \ 10^{-3}$ Torr. For a fixed value of the discharge current, three modes of the positive column were observed depending on the tube temperature [27, 28, 36], specifically, a constricted PC, a wide homogeneous PC, and a PC with a filament. The first PC mode occurred at a high DT wall temperature, i.e., under

a relatively high density of Cs vapors. At the tube wall temperature exceeding 110°C the positive column of a Cs-Xe discharge was constricted and occupied only part of the cross section of the discharge tube. For the first PC mode, the DC electric field in the positive column $E_0$ was less than 0.8 V/cm. Emission lines of cesium atoms dominated in the spectrum of visible light from the constricted PC. As the tube temperature decreased, the width of the positive column and the DC electric field increased. The second mode of the PC was observed for the tube wall temperature ranging from 100°C to 80°C. At these temperatures, the homogeneous positive column filled the entire cross section of the discharge tube. The aperture of the homogeneous plasma slab was approximately equal to the operating aperture of the discharge tube windows $10 \times 8$ cm$^2$ (see Figure 2(a)). The DC electric field in the homogeneous PC increased from 0.9 to 1.7 V/cm when the tube temperature decreased from 100°C to 80°C. If the discharge tube was cooled further, a bright filament 5 mm in diameter appeared. The filament was directed along the discharge current. The rest of the tube cross section was filled with a homogeneous positive column. The positive column with the filament was the third PC mode [27, 36–38]. Xenon was excited and ionized in the filament, and bright xenon atom lines along with the cesium atom lines were observed in its emission spectrum.
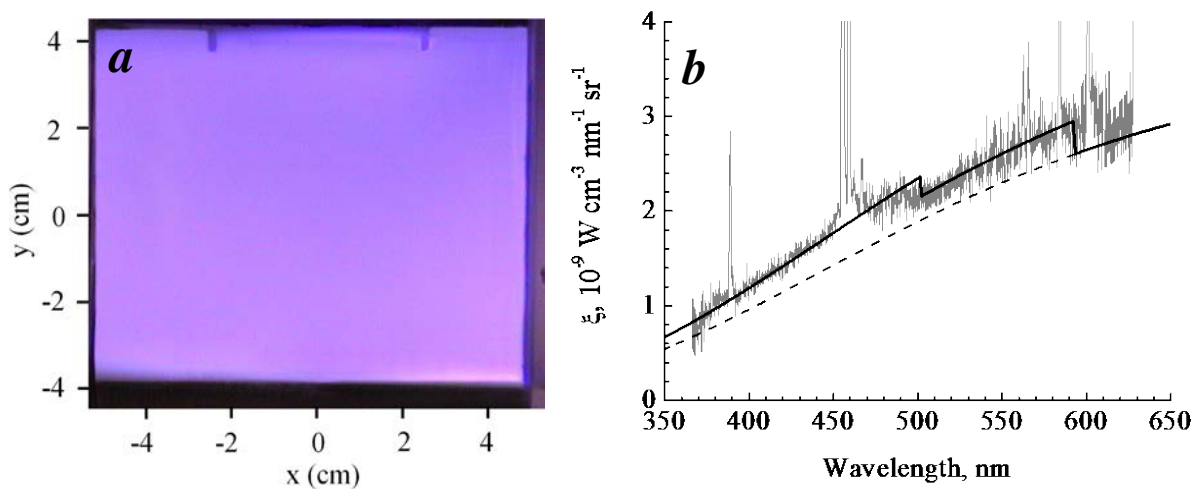


**Figure 2.** (a) A photo of the homogeneous positive column of a Cs-Xe discharge (the second PC mode). (b) Spectrum of the light emitted from the homogeneous positive column of a Cs-Xe discharge in the visible region.

The decrease in the cesium density with decreasing DT temperature was the main reason for the deconstriction of the PC of a Cs-Xe discharge and the transition from the first to the second PC mode. The electron temperature in the first and second PC modes is too low for a considerable ionization of xenon, and the main ion species in these PC modes are cesium atomic ions Cs$^+$ [27, 28, 35]. The ionization degree of cesium in the Cs-Xe discharge plasma is high and the number density of positive cesium ions is more than 80% of cesium [35]. Therefore, a decrease in the cesium density with decreasing tube temperature results in an almost proportional decrease in the density of cesium atomic ions. Owing to the plasma quasineutrality, the electron density in the PC is equal to the density of cesium atomic ions; hence, a decrease in the tube temperature also leads to a decrease in the electron density in the PC of the Cs-Xe discharge. For a fixed value of the discharge current, a decrease in the electron number density in the PC

plasma leads to an increase in the transverse dimension of the current flow region, i.e., deconstriction of the PC. The positive column ceased to become wider with decreasing tube temperature only when the PC plasma filled entirely the internal cross section of the quartz cell.

Gray thin line in Figure 2(b) shows emission spectrum of the homogeneous positive column (second PC mode) in the visible region for the discharge current density $j$=0.1 A/cm$^2$ and DC electric field $E_0$ = 1.1 V/cm. This spectrum clearly reveals the continuum and the cesium atom emission lines. The electron temperature $T_e$ in the thermal nonequilibrium PC plasma was measured using the spectra of visible continuum radiation from the PC of a Cs-Xe discharge [27, 28, 39–41]. In the homogeneous positive column $T_e$ rose from 0.4 ± 0.05 to 0.5 ± 0.05 eV as the DC electric field increased from 1 to 1.4 V/cm. For the second PC mode, the DC electric field, electron temperature, and density vary in space only weakly, except for the narrow layers near the tube walls: $E_0(x, y) \approx$ const, $T_{e0}(x, y) \approx$ const, and $N_{e0}(x, y) \approx$ const, where the subscript zero denotes the values of the parameters in the absence of MMW exposure. Using the results of $E_0$ and $T_{e0}$ measurements, the electron number density $N_{e0}$ in the positive column was determined by the equation $N_{e0} = j / e\mu(T_{e0})E_0$ [42], where $e$ is the electron charge, $\mu(T_e)$ is the DC electron mobility, and $j$ is the discharge current density equal to $j = J / S$ ; here $S$ is the internal cross-sectional area of the quartz cell.

The wide homogeneous plasma slab, i.e., the second PC mode, was used as an imager for MM waves. In the experiments on imaging of MMWs, the discharge current was 1.5 A, and the DT temperature was about 90°C. When there were no incident MMWs, the DC electric field in the PC was equal to $E_0$ = 1.15 ± 0.05 $V / cm$, the electron temperature was $T_{e0}$ = 0.47 ± 0.03 eV, and the electron density was $N_{e0}$ = (2.7 ± 0.3)•10$^{12}$ cm$^{-3}$. The electron density in the homogeneous PC of a Cs-Xe discharge was much less than the critical density for MMW frequency band, so reflection of the MM waves from the plasma was weak (less than 1%) [42]. The absorption coefficients $\gamma_0 = \gamma(T_{e0})$ of the PC plasma for Ka and D band MM waves were equal to 0.3 cm$^{-1}$ and 0.01 cm$^{-1}$, respectively [27, 29].

## 3. Evaluation of the performance of the VCRD technique

The MMW effects on a slab of the PC of a Cs-Xe discharge have been experimentally studied to develop the VCRD technique for imaging of MMWs and determine its basic characteristics. The model experiments[1] on imaging of the field patterns of horn antennas and quasioptical beams have been performed. Figure 3 shows a layout of the experiments on imaging of the near-field patterns at the output of a MMW horn antenna. The images of the plasma slab were captured by a black and white charged coupled device (CCD) camera. The data from the CCD camera were processed with a computer. A set of optical filters rejecting atomic emission lines and transmitting the continuum in the visible region was placed in front of the camera lens.

---

1 In the model experiments, the MMW field profiles have been known from calculations or measurements by conventional techniques.

The filter set had a transmissivity of less than 0.1% in the near IR range and in the region from 450 to 460 nm, where the bright lines of the second resonance doublet of cesium occur (see Figure 2(b) and refs. [27, 28]). The contribution of atomic-line intensity into the wavelength-integrated intensity of the transmitted light was a few percent only.
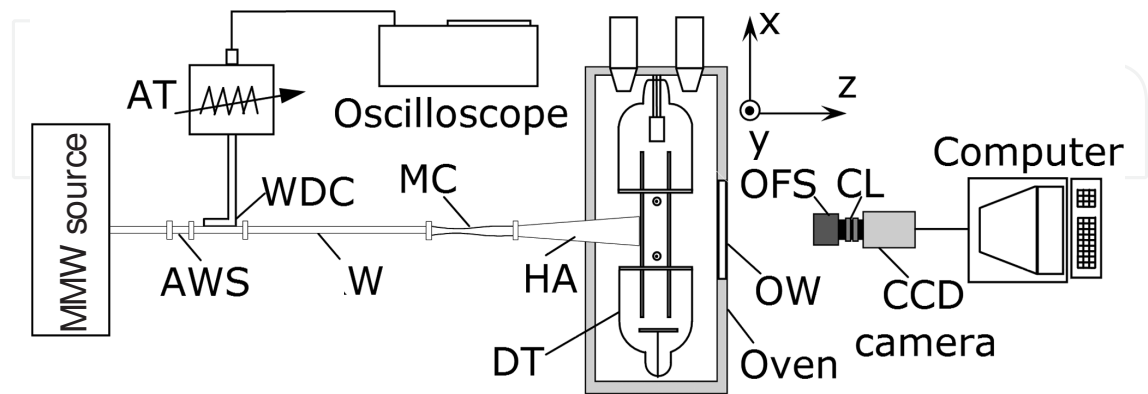


**Figure 3.** Schematic diagram of the experimental setup (top view) for imaging of the field patterns at the output of a horn antenna; W: waveguide; AWS: waveguide section with MMW absorber; WDC: waveguide directional coupler; AT: MMW attenuator; MC: mode converter; HA: horn antenna; DT: discharge tube; OW: oven window; OFS: optical filter set; CL: camera lens.

To evaluate the microwave-induced variation in the VCR energy flux $\Delta S_C(x, y)$, the background VCR energy flux $S_{C_0}(x, y)$ was subtracted from the VCR energy flux $S_C(x, y)$ : $\Delta S_C(x, y) = S_C(x, y) - S_{C_0}(x, y)$. The VCR energy flux $S_C(x, y)$ was obtained using the CCD camera frame simultaneous with the MMW pulse, and the background VCR energy flux $S_{C_0}(x, y)$ was obtained using the CCD camera frame preceding the MMW pulse. When the VC emissivity is time-independent during the camera exposure time $\tau_e$, the VCR energy flux is equal to $S_C(x, y) = \tau_e I(x, y)$, where $I(x, y)$ is the intensity of the visible continuum radiation, and the relative variation in the VCR intensity is equal to the relative variation in the VCR energy flux $\Delta I(x, y) / I_0(x, y) = \Delta S_C(x, y) / S_{C_0}(x, y)$, where $\Delta I(x, y) = I(x, y) - I_0(x, y)$ ; here $I_0(x, y)$ is the background VCR intensity.

Study of the millimeter wave effect on the homogeneous positive column of a Cs-Xe discharge was performed using conical horn antennas (see Figure 3) excited by the $TE_{11}^O$ mode of a circular waveguide [27]. A 35.4-GHz magnetron was used as a source of MM waves. The magnetron supplied coherent radiation with an output power of up to 20 W in the long-pulse mode. The MMW pulse length was up to 100 ms, and the pulse leading edge was less than 0.1 μs. Mode converters were used to transform the $TE_{10}$ mode of a rectangular waveguide into the $TE_{11}$ mode of a circular waveguide [43, 44]. The conical horns had aperture radii from 10 to 30 mm. The MMW electric field polarization in the vicinity of the beam axis was directed along the $x$ coordinate (see Figure 3). The discharge tube window was attached directly to the output of a horn antenna, and the spatial distribution of the MMW intensity was measured in the near-field region. A set of rectangular waveguide sections with MMW absorber was used to decrease

the power of millimeter waves that are incident on the PC plasma. By using the waveguide section with a MMW absorber, the MMW power can be decreased up to 15 dB with discrete steps of about 3 dB. The MMW power was also varied smoothly by changing voltage and current supplied to the magnetron. For relative measurements of the radiated power, a small part of the MMW radiation was branched to the calibrated attenuator by a waveguide directional coupler. The output signal from the attenuator was detected using a MMW detector and measured using an oscilloscope.

When the MMW intensity $W$ exceeded the breakdown threshold $W_{Br}$, a microwave-induced breakdown of the PC slab occurred, and bright thin filaments were observed in the plasma area affected by a MMW beam. The filaments were elongated in the direction of the MMW electric field. Figure 4(a) shows the spatial distribution of the VCR energy flux variation when there was a microwave-induced breakdown of the plasma slab. The threshold value of the microwave breakdown for the Ka-band was equal to about 4 W/cm² for $E_0$ = 1.1 V/cm. It decreased to approximately 2 W/cm² for $E_0$ = 1.5 V/cm. When $W > W_{Br}$, MMW heating increases the electron temperature so that excitation and ionization of xenon become significant. Ionization of xenon is the major cause of ionization instability of the homogeneous PC and the appearance of filaments with a high electron density, i.e., a microwave breakdown of the plasma slab [35].
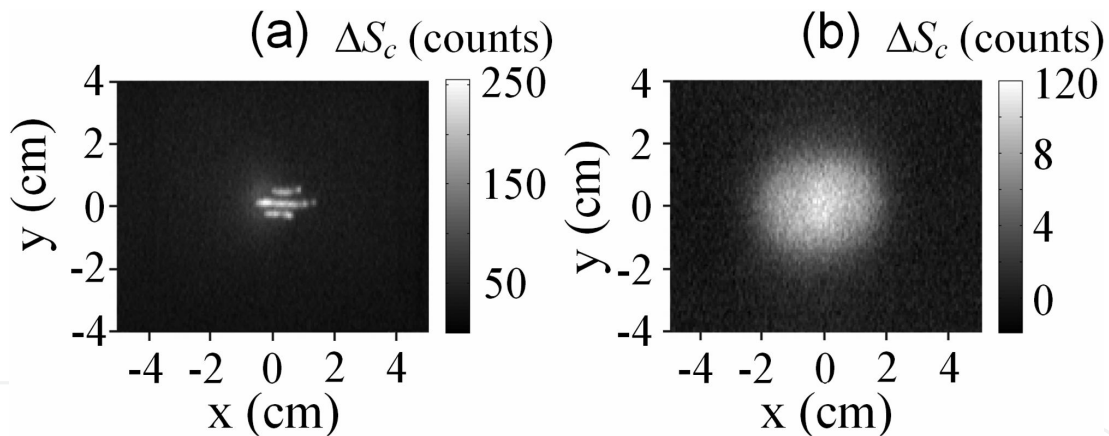


**Figure 4.** Spatial distribution of the VCR energy flux variation at the output of a conical horn antenna excited by the $TE_{11}^O$ mode for the MMW intensities (a) above and (b) below the microwave-induced breakdown threshold of the plasma slab.

Figure 4(b) shows a 2D distribution of the VCR energy flux variation $\Delta S_C(x, y)$ at the output of a conical horn antenna,[2] when the MMW intensity in the field maximum was less than the microwave breakdown threshold. The horn antenna with the taper angle of 5° and output aperture radius $R_h$ = 22.5 mm was excited by the $TE_{11}^O$ mode. The CCD camera exposure time was equal to 200 μs. The spatial distribution of the VCR energy flux variation is smooth, and

2 The coordinates are denoted $x$ and $y$ in the reference frame, whose origin coincides with the center of the DT window, and the coordinates are denoted $x'$ and $y'$ in the reference frame, whose origin coincides with the MMW beam center.

it resembles the intensity profile for the $TE_{11}^{O}$ mode (see Figure 4(b)). Using the same conical horn excited by the $TE_{11}^{O}$ mode, the dependences of the relative VCR intensity variation $\Delta I(0, 0)/I_0(0, 0) = \Delta S_C(0, 0)/S_{C_0}(0, 0)$ on the intensity of millimeter waves incident on the plasma slab $W(0, 0)$ was measured. The CCD camera exposure time was 100 and 200 μs. The measured dependence of $\Delta I/I_0$ on $W/W_{Br}$ is shown in Figure 5 by diamonds. In the range of MMW intensities from 0 to $W_{Br}$, the second-order polynomial function fits the dependence $\Delta I(W)/I_0$ with an accuracy of up to a few percent (black solid line in Figure 5). For the MMW intensity range $0 < W < W_{Br}/3$, the value of $\Delta I$ could be considered approximately directly proportional to the intensity of millimeter waves (with an accuracy of about 10%). If the MMW intensity is below the breakdown level, MMW beam profile can be obtained from the distribution of the VCR intensity variation using the dependence of $\Delta I/I_0$ on $W$.
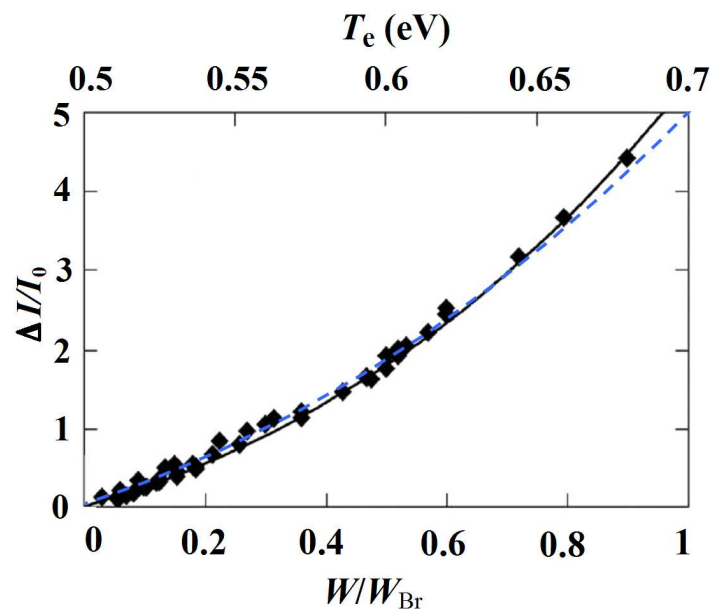


**Figure 5.** Experimental dependence of the relative VCR intensity variation as a function of the intensity of MM waves incident on the plasma slab (black diamonds), and calculated dependence of the relative VCR intensity variation as a function of the electron temperature (blue dashed line).

The data of the experiment on the imaging MMW intensity profile at the output of the conical horn antenna with an aperture radius of 22.5 mm excited by the $TE_{11}^{O}$ mode (see Figure 4(b)) were compared with the calculated spatial distribution of the EM wave intensity for the $TE_{11}^{O}$ mode of a circular waveguide of the same radius. For $x' = 0$, the calculated EM wave intensity decreases as a function of $|y'|$ without discontinuities from the maximum value $W_m$ at the center of the waveguide to zero near the waveguide wall, i.e., for $y' = \pm 22.5$ mm [43, 44]. The measured dependences of the VCR intensity variation vs. coordinate $y'$ for $x' = 0$ were in good agreement with the calculated spatial distribution of the EM wave intensity $W(x' = 0, y')$. For $y' = 0$, the measured dependence of the VCR intensity variation vs. the coordinate $x'$ was

different from the calculated spatial distribution of the EM wave intensity for the $TE_{11}^{O}$ mode $W(x', y'=0)$ in the regions near $x' = \pm 22.5$ mm. For $y' = 0$ the sharp edges of the MMW intensity distribution near the waveguide wall were blurry at the image. The blurring effect appeared due to the diffraction of MMWs at the edge of a horn antenna and electron heat conduction (see Section 4.2).

The experiments on imaging of the MMW field profiles at the output of the conical horn antennas excited by the axially symmetric $TE_{01}^{O}$ mode of a circular waveguide were carried out in ref. [27]. The same 35.4 GHz long-pulse magnetron was used in these experiments. The $TE_{10}$ mode of a rectangular waveguide was transformed into the $TE_{01}^{O}$ mode of a circular waveguide by a Marier transducer (see Figure 3). Figure 6(a) shows a 2D distribution of the MM wave-induced variation of the VCR intensity $\Delta I(x, y)$ at the output of a conical horn with a taper angle of $6^{o}$ and output aperture radius $R_h = 28$ mm. The MMW intensity at the field maximum was $W_m \approx 1$ W/cm$^2$. The CCD camera exposure time was 100 μs. The obtained pattern of the VC glow corresponds to the $TE_{01}^{O}$ mode with a small admixture of other modes[3] (see Figure 6(a)). Black lines in Figures 6(b) and 6(c) show the dependence of the VCR intensity variation under the MMW effect vs. the coordinates $y$ for $x' = 0$ and $x$ for $y' = 0$, respectively. For the $TE_{01}^{O}$ mode, the dependence of the MMW intensity on the radius $r = \sqrt{(x')^2 + (y')^2}$ is $W(r) \approx W_m \cdot [1.72 J_1(3.832 r / R_h)]^2$ for $r < R_h$, where $J_1$ is a first-order Bessel function and $R_h =$ is the radius of a circular waveguide or the aperture of a conical horn [43, 44]. Gray lines in Figures 6(b) and 6(c) show the function $W(r)$. The function $W(r)$ fits well with the measured dependences $\Delta I(x, y'=0)$ and $\Delta I(x'=0, y)$. However, the intensity variation of the VC radiation from the plasma region near the axis of the MMW beam $\Delta I(x'=0, y'=0)$ was equal to 15% of the VC intensity variation at the field maximum $\Delta I_m$ (see Figures 6(b) and 6(c)), while the MMW intensity at the beam center $W(0, 0)$ is equal to zero. Thin solid line in Figure 6(d) shows the dependence of the VCR intensity variation under the MMW effect vs. the coordinate $x'$ for $y' = 0$, which was obtained for a conical horn with an aperture radius $R_h = 20$ mm. For a horn antenna of this aperture size, $\Delta I(0, 0) / \Delta I_m$ was about 25%. When conical horns with smaller aperture radii were used, the relative value of the VCR intensity variation in the beam center $\Delta I(0, 0) / \Delta I_m$ increased, i.e., the central deepening became shallower. Thus, a violation of the local relation between the intensity of the plasma VC radiation and the MMW intensity was observed in these experiments. The causes of the nonlocality of microwave-induced variations in the intensity of the VC radiation from a medium-pressure cesium-xenon DC discharge are discussed in Section 4.2.

An experiment on imaging of the Ka-band quasioptical millimeter-wave beam using the VCRD technique is described in ref. [27]. The quasi-Gaussian MMW beam was focused by a double-

---

3 An experiment showed that the dependence of the VCR intensity on the azimuthal coordinate (see Figure 6(a)) is caused by the admixture of other waveguide modes excited in a conical horn, but not the spurious plasma effect. In this experiment, a rectangular waveguide, which was twisted through an angle of approximately 90°, was installed before the Marier transducer. The image of the spatial distribution of the MMW intensity was also rotated through an angle 90° in the same direction.
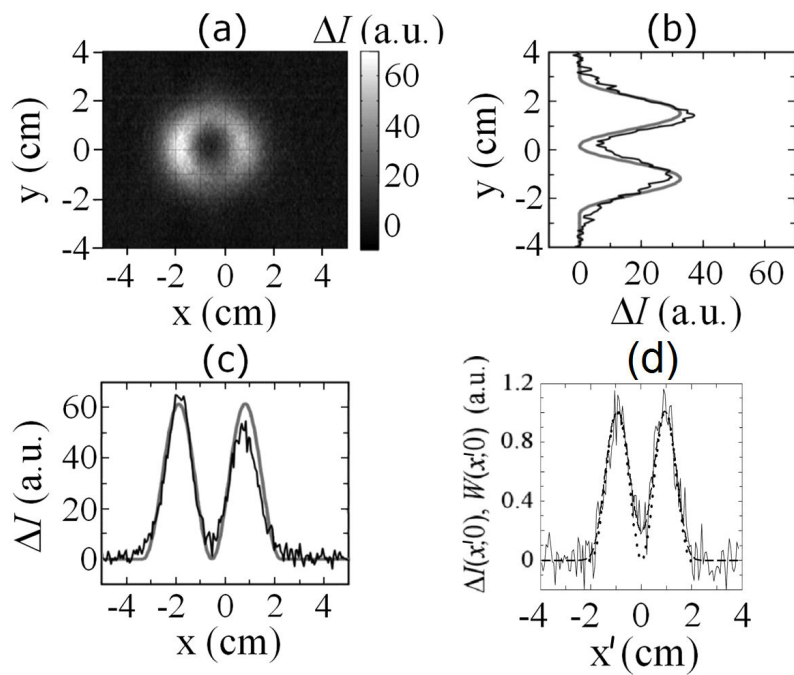
**Figure 6.** Spatial distributions of the VCR intensity variation at the output of the conical horn antennas excited by the TE$_{01}^{O}$ mode. (a) Two-dimensional distribution of the VCR intensity variation. (b) and (c) Measured dependence of the VCR intensity variation (black lines) and calculated dependences of the MMW intensity variation (gray lines) vs. the coordinates $y$ for $x' = 0$ (b) and $x$ for $y' = 0$ (c) for a horn with the aperture radius $R_h = 28$ mm. (d) Measured (solid gray line) and calculated (dashed black line) dependences of the VCR intensity variation vs. the coordinates $x'$ for $y' = 0$ for a horn with the aperture radius $R_h = 20$ mm. Calculated dependence of the MMW intensity variation vs. $x$ for $y' = 0$ (dotted line).

convex Teflon lens 20 cm in diameter and a focal length of 32 cm at the center of the plasma slab. The width of the MMW beam (FWHM) in the focus was approximately 2.5 cm. The distribution of the VCR intensity variations in the focal plane of the lens was compared with the MMW field profile. The MMW intensity profile was measured by a mechanically scanned receiver with calibrated MMW detector. The patterns measured by the two techniques coincided within the limits of the random experimental error. Thus, model experiments on imaging of the field profiles of horn antennas and quasioptical beams have demonstrated that the VCRD technique can be used for good-quality imaging of Ka-band MMW beams.

The response time of the VCR intensity to the variation in the MMW intensity was measured using a photomultiplier tube (PMT) [27]. In these experiments, the photomultiplier tube was set in place of the CCD camera (see Figure 3). The optical filter set rejecting atomic emission lines and transmitting the VC radiation from the PC of a Cs-Xe discharge was mounted before the PMT input window. The temporal resolution of the setup used for recording of the VCR intensity time history was less than 50 ns. After the MMW radiation was switched on, the measured waveform of VCR intensity fit well with the exponential time dependence:

$$\Delta I = \Delta I_{\infty} \left\{ 1 - \exp\left[ -(t - t_0)/\tau \right] \right\}, \tag{1}$$

where $\Delta I_\infty$ is the VCR intensity variation, $t_0$ is the time point at which the MMW pulse was switched on, and $\tau$ is the characteristic time of VCR intensity variation. The VCR response time was about $\tau = 0.8 \pm 0.1$ μs. This time is approximately equal to the time of the electron temperature variation in the PC plasma (see Section 4.2 and refs. [27, 35]). Thus, it was shown that the VCRD technique for MMW imaging is very rapid and its temporal resolution was less than 1 μs.

In the experiments on imaging of Ka-band MM waves using the VCRD technique, a single-shot signal to noise ratio (SNR) was about one when the MMW intensity was $W \approx 1$ W/cm$^2$ and the CCD camera exposure time was set at 10 μs [27]. Thus, in the Ka-band, a single-shot threshold energy flux sensitivity (SNR = 1) of about 10 μJ/cm$^2$ was achieved. In the performed experiments, the energy flux sensitivity was restricted by the noise performance of the CCD camera. The actual sensitivity of the VCRD technique is determined by fluctuations of the parameters of the PC of a Cs-Xe discharge, primarily, by the fluctuations of the electron temperature in the plasma [45]. Estimated sensitivity of the VCRD technique is higher by at least an order than the sensitivity achieved in the experiments. Further study is required for more accurate determination of the VCRD technique sensitivity.

The VCRD technique can be used to image the intensity patterns of the EM waves in a wide band from short-wavelength centimeter to submillimeter waves. When the MMW frequency increases, the plasma becomes more transparent for MMWs due to a decrease in the MMW absorption coefficient, and the MMW effect on the plasma parameters decreases [27, 29]. At the xenon pressure of tens of Torr, the electron-Xe atom collision frequency for the momentum transfer was much less than the angular frequency $\omega$ of MM waves [27, 29]. In this case, the scaling law for the efficiency of electron heating under the MMW effect is $\Delta T_e \propto W / \omega^2$, where $\Delta T_e$ is the electron temperature variation. Therefore, on passing from long-wavelength to short-wavelength millimeter waves, the sensitivity of the technique decreases if the identical systems are used for VC radiation recording. The threshold of the microwave breakdown of a plasma slab is significantly increased in a short MMW band. For example, on passing from Ka-band to D-band the threshold of the microwave breakdown of a plasma slab increases to the value of the order of 100 W/cm$^2$, but the energy sensitivity of the VCRD technique deteriorates to the level of hundreds of μJ/cm$^2$.[4]

The ability to image the intensity profiles of short-wavelength MM waves using the VCRD technique was demonstrated in refs. [29, 30]. Thus, the wide frequency band of the technique has been confirmed. In paper [29], the intensity profile of the D-band MMW beam was measured at the output of a corrugated conical horn antenna. The arrangement of this model experiment was similar to the arrangement of the experiment on imaging of Ka-band MMWs at the output of conical horn antennas (see Figure 3). A pulsed F- and D-band orotron OR-180 was used as a source of MM waves (see Section 5.1 and ref. [46]). In this experiment, the orotron radiation frequency was 140 GHz. The maximum orotron power was about 0.6 W. The MMW pulse length was 3 ms, and the pulse repetition rate was 10 Hz. The corrugated conical horn was fed by the orotron through an E-band rectangular waveguide and a down taper. The

---

4 In the D band, a single-shot energy flux sensitivity of about 200 μJ/cm$^2$ was demonstrated [29, 30].

output diameter of the corrugated horn was 16 mm, and its length was about 90 mm. The discharge tube window was attached to the output of the horn. The corrugated horn forms a high-quality axially symmetric Gaussian beam [47]. The width (FWHM) of the Gaussian MMW beam in the middle plane of the plasma slab was equal to 7.8 mm. The MMW electric field vector at the output of the horn was directed along the $y$ coordinate. Figure 7(a) shows the 2D distribution of the VCR intensity variation induced by the MMW beam, which was measured at the output of the corrugated conical horn. The solid lines in Figures 7(b) and 7(c) show the VCR intensity variation as functions of the $x'$ and $y'$ coordinates, respectively. The CCD camera exposure time was 2 ms. To improve the SNR, the images of the MMW field pattern (see Figure 7) were averaged using 300 camera frames. The image was broader than the MMW beam by approximately 1 mm, and it had no axial symmetry in the region of the beam tail.[5] The causes of the broadening of the MMW beam images and their axial asymmetry are discussed in Section 4.2. The MMW intensity profile in the focal region of a Teflon conical lens (axicon) was imaged by the VCRD technique in refs. [29, 30]. A 140 GHz Gaussian EM beam, which is radiated from a corrugated conical horn and collimated by a Teflon lens, was incident on the axicon. The corrugated horn was fed from orotron OR-180. The 2D intensity profiles of the focused MMW beam were imaged at various distances from the axicon. It has been shown that the axicon forms a beam with the width (FWHM) of a focal spot of less than 3 mm and a focal length of about 10 cm. The imaging of the profiles of the MMW beams, which were formed by a corrugated horn antenna and an axicon, demonstrates that the VCRD technique can be used for imaging of MMW beams having a width of more than several millimeters.
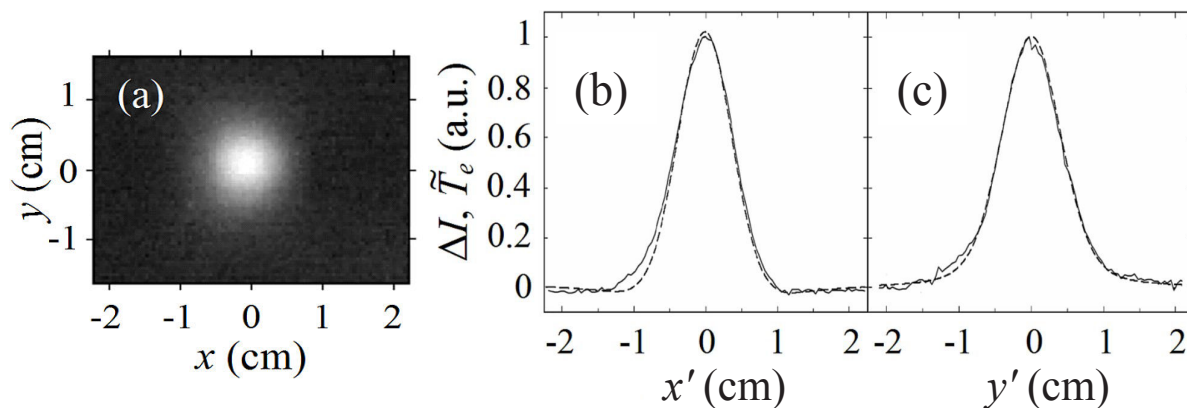


**Figure 7.** (a) 2D distribution of the VCR intensity variation at the output of a D-band corrugated conical horn. (b) and (c) Measured dependences of the VCR intensity variation $\Delta I$ (solid lines) at the output of a corrugated conical horn and calculated electron temperature perturbation $\tilde{T}_e$ (dashed lines) on the coordinates $x'$ for $y' = 0$ (b) and $y'$ for $x' = 0$ (c).

---

[5] When a section of the D-band rectangular waveguide twisted by an angle of 90° was installed before the corrugated conical horn, the horn rotated around its axis by 90°, and the MMW polarization in the Gaussian beam also changed from direction along the $y$-axis to direction along the $x$-axis. However, this rotation does not change the shape of the image of the MMW beam.

## 4. Fundamentals of the VCRD technique

This section discusses the nature of the visible continuum radiation from the PC of a Cs–Xe discharge and the mechanism responsible for the VCR intensity variation under the MMW effect. The relationship of the spatial distributions of the VC emissivity variation and intensity of MMW radiation incident on the plasma slab is also studied. The factors determining the spatial and temporal resolution of the VCRD technique are discussed.

### 4.1. Mechanism of the MMW effect on the intensity of the VC radiation from the PC of a Cs-Xe discharge

The nature of the visible continuum radiation from the positive column of a Cs-Xe discharge for plasma parameters that are typical for the MMW imaging experiments was studied in refs. [27, 28]. It was shown that the electron-Xe atom bremsstrahlung continuum (e-Xe BC) and the cesium recombination continuum (RC) give the main contributions to the visible continuum radiation from the PC of a Cs-Xe discharge. The VC emission coefficient $\xi(\lambda)$ is equal to the sum of emission coefficients for the electron-Xe atom bremsstrahlung continuum $\xi_{e-Xe}^{BC}(\lambda)$ [39–41, 48–50] and the cesium recombination continuum $\xi^{RC}(\lambda)$ [39, 51]:

$$\xi(\lambda) = \xi_{e-Xe}^{BC}(\lambda) + \xi^{RC}(\lambda). \tag{2}$$

Visible RC radiation originates from recombination of the electrons and Cs$^+$ ions into $6P$ and $5D$ electronic states of cesium (blue and yellow cesium RC, respectively) [51]. Thus, the emission coefficient for the recombination continuum of cesium in the visible region is equal to $\xi^{RC}(\lambda) = \xi_{6P}^{RC}(\lambda) + \xi_{5D}^{RC}(\lambda)$, where $\xi_{6P}^{RC}(\lambda)$ and $\xi_{5D}^{RC}(\lambda)$ are the emission coefficients for $6P$- and $5D$-recombination continua of cesium, respectively. The emission coefficients of the blue and yellow cesium recombination continua for $\lambda < hc/E_n$ are equal to [27, 39, 51]

$$\xi_n^{RC}(\lambda) = A\lambda^{-3}\sqrt{\varepsilon}\,\sigma_n(\varepsilon)N_+N_ef_0(\varepsilon), \tag{3}$$

where $n$ means $6P$ or $5D$, $E_n$ is the binding energy of atomic state $n$, $h$ is the Planck constant, $c$ is the speed of light, $\lambda$ is the wavelength of the emitted light, $A$ is a constant which is equal to approximately $6 \cdot 10^{-36}$ kg$^{3/2}$m$^6$s$^{-4}$sr$^{-1}$, $\varepsilon$ is the electron energy, $\sigma_n(\varepsilon)$ is the cross section of radiative recombination into the $n$th electronic state of a cesium atom, $N_+$ is the number density of the Cs$^+$ ions ($N_+ \approx N_e$), and $f_0(\varepsilon)$ is an isotropic component of the electron energy distribution function (EEDF). For RC radiation, the relationship between the free electron energy and the light wavelength is $\varepsilon = hc/\lambda - E_n$. For $\lambda > hc/E_n$, $\xi_n^{RC}(\lambda)$ is equal to zero. The emission coefficient of the e-Xe BC is given by [27, 28, 40]

$$\xi_{e-Xe}^{BC}(\lambda) = C\frac{N_eN_{Xe}}{\lambda^2}\int_{\frac{hc}{\lambda}}^{\infty}\sqrt{\varepsilon - \frac{hc}{\lambda}}\left\{\varepsilon\sigma_t\left(\varepsilon - \frac{hc}{\lambda}\right) + \left[\varepsilon - \frac{hc}{\lambda}\right]\sigma_t(\varepsilon)\right\}f_0(\varepsilon)d\varepsilon, \tag{4}$$

where $C$ is a constant which is equal to approximately $0.9\,\mathrm{sr^{-1}kg^{-1/2}m}$, $N_{Xe}$ is the Xe atom number density, and $\sigma_t(\varepsilon)$ is the momentum transfer cross section for the electron scattering from a xenon atom. Thick solid line in Figure 2(b) shows the VC emission coefficient $\xi(\lambda)$, which was calculated by Eqs. (2)–(4) for $N_{e0} = 2.5\ 10^{\cdot 12}\ \mathrm{cm^{-3}}$ and EEDF with the effective electron temperature $T_{e0} = 0.47$ eV [28]. The results of calculations agree well with the measured VC emission spectra. Dashed line in Figure 2(b) shows calculated e-Xe BC emission coefficient for the same plasma parameters. In the visible region, the intensity of e-Xe BC radiation is several times greater than the maximum intensity of the cesium RC radiation.

The intensity of the visible continuum from the PC of a Cs-Xe discharge rises when the millimeter waves incident on the plasma slab or the DC electric field in the PC plasma increases. It follows from Eqs. (3) and (4) that the rise in the VCR intensity can be caused by an increase in the electron number density or by EEDF variation. The electron-density variation induced by the MMW or DC electric field cannot explain the observed increase in the VCR intensity. Firstly, due to a high ionization degree of cesium in the homogeneous positive column, the microwave-induced variation in the electron density is relatively small ($\Delta N_e / N_{e0} << 1$) [35], whereas the effect of watt-scale Ka-band MMWs on the PC plasma increases the VCR intensity significantly ($\Delta \xi / \xi \sim 1$) (see Figure 5). Secondly, the characteristic time of the electron density variation [35, 36] is several orders of magnitude longer than the VCR response time (see Section 3). Thirdly, when the discharge tube temperature was decreased, the electron number density $N_{e0}$ in the homogeneous PC also decreased, whereas the VCR intensity and the DC electric field $E_0$ increased [28]. Hence, the VCR intensity variation is caused by the EEDF variation resulting from the MMW or DC electron heating. Using Eqs. (2)–(4), the VC emission coefficient were calculated for different electron temperatures in the homogeneous PC plasma. The electron density was assumed constant. Solid lines in Figure 8 show the continuum emission coefficient $\xi(\lambda)$ in the visible region calculated for 45 Torr xenon, $N_e = 2.5 \bullet 10^{12}\ \mathrm{cm^{-3}}$ and the EEDF with the effective electron temperatures $T_e = 0.45, 0.5, 0.55$, and 0.6 eV. Dashed lines in Figure 8 show the e-Xe BC emission coefficient $\xi_{e-Xe}^{BC}(\lambda)$ calculated for the same plasma parameters. In the visible region, the wavelength-integrated emission coefficient for the e-Xe BC radiation exceeds the wavelength-integrated emission coefficient for the cesium recombination continuum by about one order of magnitude. Figure 8 demonstrates that the increase in the VC emissivity is caused by the e-Xe BC emissivity increase due to an additional electron heating and is not caused by an increase in the cesium recombination continuum emissivity as was believed earlier [31]. As the electron temperature rises from $T_e = 0.45$ to 0.6 eV, the intensity of the e-Xe BC in the visible region increases more than fourfold.

Explanation of the phenomenon of the increase in the e-Xe BC radiation intensity in the visible region induced by the electron heating is quite obvious. Bremsstrahlung photons with wavelength $\lambda$ can be emitted only by electrons with kinetic energies greater than the energy of a light quantum, i.e., $\varepsilon > hc / \lambda$. The visible light wavelengths ranging from 620 nm to 410 nm correspond to photon energies from 2 to 3 eV. The bremsstrahlung photons with such an energy can be emitted by the electrons from the tail of the EEDF ($\varepsilon > 2$–$3\,\mathrm{eV}$) because the electron temperature in the homogeneous PC of a Cs-Xe discharge is from 0.4 to 0.8 eV. Thus, the
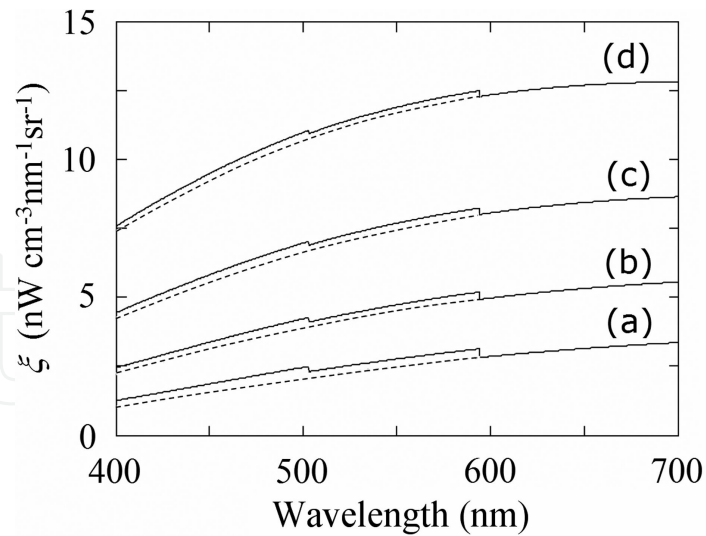
**Figure 8.** The visible continuum (solid line) and e-Xe bremsstrahlung continuum (dashed line) emission coefficients vs. wavelength for effective electron temperatures (a) 0.45, (b) 0.5, (c) 0.55, and (d) 0.6 eV.

increase in the e-Xe bremsstrahlung radiation intensity in the visible region is caused primarily by an increase in the fast electron number density, which results from the additional electron heating induced by the MMW or DC electric field. The bremsstrahlung cross section for electron-atom collisions increases with increasing electron energy (see Eq. (4) and refs. [40, 50]). This is another cause of the increase in the VC brightness due to DC- or microwave-induced electron heating.

Verification of the previously discussed mechanism of the electromagnetic field effect on the brightness of the visible continuum radiation from the PC of a Cs-Xe discharge was carried out in ref. [28], where the effects of the DC electric field strength and electron density on the intensity of VC radiation were studied experimentally. There was no MMW radiation incident on the plasma. The electron density was varied by changing the discharge current. The DC electric field strength was varied by changing the tube temperature for a fixed value of the discharge current. Experimental data are in a good agreement with the results of calculations done using the above model [28]. In ref. [27], the dependence of the relative intensity variation of the VC radiation from the PC of a Cs-Xe discharge, $\Delta I / I_0$, on the electron temperature was calculated. The best agreement between the results of calculations and the experimental data is achieved when it is assumed that the microwave breakdown of the plasma slab occurs at an electron temperature equal to $T_{eBr} = 0.7$ eV. Dashed line in Figure 5 shows the calculated dependence $\Delta I(T_e)/I_0$ for $T_{eBr} = 0.7$ eV.

### 4.2. Relation between spatial profiles of the VC emissivity and the MMW intensity. Spatial and temporal resolution of the VCRD technique

The causes of violation of the local relation between the visible continuum emissivity and the MMW intensity, as well as the main factors which limit the spatial resolution of the VCRD technique, were explored in ref. [29]. The emissivity of the e-Xe bremsstrahlung continuum

depends locally on the effective electron temperature $T_e(x, y, z)$ and electron density $N_e(x, y, z)$ in the PC of a Cs-Xe discharge (see Eqs. (2)–(4)). The electron density variation is relatively small in the PC plasma, and its effect on the brightness of VC radiation is not significant. The main cause of the increase in the VC intensity is the microwave-induced increase in $T_e$ (see Section 4.1). The value of $\Delta I$ is directly proportional to the local value of the electron temperature variation $\Delta T_e$ when $\Delta T_e < 0.1$ eV. Spatial profiles of the microwave-induced perturbations in the electron temperature and density in the slab of the PC of a Cs-Xe DC discharge were analytically modeled [29]. The model considers the effects of the electron heating by the DC and MMW electric field, the electron energy loss due to electron-atom collisions, electron heat conduction, diffusion, and thermal diffusion of the charged particles. The perturbations of the electron temperature induced by MMW beams which had different shapes were described by the electron-energy balance equation. Perturbation technique was used to find the solutions for this equation. It was sufficient to calculate the first- and second-order terms for the electron temperature perturbation to explain the results of the experiments. For a one-dimensional (1D) MMW beam having a width much smaller than the size of the operating aperture of a plasma slab, the spatial distribution of the electron temperature perturbation of the first order is given by the convolution of the MMW intensity $W(\zeta)$ and the line spread function (LSF) for the VCRD technique $G_e(\zeta)$ :

$$\tilde{T}_{e1}(\zeta) = \frac{2\gamma_0 \tau_\varepsilon}{3kN_{e0}} \int_{-\infty}^{+\infty} W(\hat{\zeta})G_e(\zeta - \hat{\zeta})d\hat{\zeta}. \tag{5}$$

In Eq. (5), the coordinate $\zeta$ is a linear function of $x$ and $y$, $k$ is the Boltzmann constant, and $\tau_\varepsilon \approx (2P'_0/3k)^{-1}$ is the characteristic time of electron temperature variations due to the electron energy loss in electron-atom collisions, where $P' = \partial(Q/N_e)/\partial T_e$ ; here, $Q$ is the power density of the electron energy loss due to electron-atom collisions. The line spread function for VCRD technique is in direct proportion to the electron temperature perturbation induced by an infinitely narrow 1D MMW beam with the intensity $W(\zeta) = W_m \delta(\zeta - \zeta_0)$, where $\delta(\zeta)$ is a delta function. In a first-order approximation, LSF is given by the Laplace distribution

$$G_e(\zeta) = \frac{1}{2\Lambda_T} \exp\left(-\frac{|\zeta - \zeta_0|}{\Lambda_T}\right); \tag{6}$$

here $\Lambda_T = (2\tau_\varepsilon \chi_0 / 3k)^{1/2}$, where $\chi$ is the electron heat conduction coefficient divided by the electron density. For a xenon pressure of 45 Torr and an electron temperature of 0.5 eV, $\Lambda_T$ is equal to about 1.5 mm, so the width of the line spread function (FWHM) equals to approximately 2 mm. When the plasma slab is affected by a two-dimensional beam, whose width is significantly smaller than the aperture sizes of the discharge tube, the electron temperature

perturbation of the first order is given by a 2D convolution of $W(x, y)$ with a modified Bessel function of the second kind of order zero $K_0(r / \Lambda_T)$,

$$\tilde{T}_{e1}(x,y) = \frac{\gamma_0}{2\pi N_{e0}\chi_0} \int\limits_{-\infty}^{\infty} \int\limits_{-\infty}^{\infty} W(\hat{x}, \hat{y}) K_0(\xi/\Lambda_T) d\hat{x} d\hat{y}; \tag{7}$$

where $\xi = \sqrt{(x-\hat{x})^2 + (y-\hat{y})^2}$. It follows from Eqs. (5) to (7) that the value of spatial broadening of the MMW beam image is determined by a parameter $\Lambda_T$, which depends on the electron heat conduction coefficient and the time of electron energy relaxation due to electron-atom collisions. Therefore, at a first-order approximation, the nonlocality of the microwave-induced variation in the intensity of the VC radiation is caused by the electron heat conduction effect. The electron heat conduction restricts the spatial resolution of the VCRD technique. Using Eq. (7), one can find that the plasma imager with aperture dimensions of about 10 cm has an equivalent number of effective sensor elements of the order of one thousand.

The calculations of the microwave-induced electron temperature perturbation based on the above-described model were compared with the data of the experiments on imaging of 34.5GHz MMW field profiles at the output of conical horn antennas with different aperture radii, which were excited by the $TE_{01}^O$ mode (see Section 3). The dashed line in Figure 6(d) shows the calculated dependence of the first-order perturbation of the electron temperature on transverse coordinate $r$ for $R_h = 20$ mm. The calculated dependence fits well with the measured spatial distributions of the VC brightness variations. Figure 7 allows one to compare the data of the experiment on imaging of a D-band MMW beam at the output of the corrugated conical horn and the calculated profiles of the electron temperature perturbation induced by a Gaussian MMW beam with a width of 7.8 mm [29]. The dashed lines in Figures 7(b) and 7(c) show the calculated dependences $\tilde{T}_e = \tilde{T}_{e1} + \tilde{T}_{e2}$ on coordinates $x$ and $y$, respectively, wher $\tilde{T}_{e2}$ is the second-order perturbation of the electron temperature. The calculations fit well with the experimental data. Figures 7(b) and 7(c) show that the calculated distributions of the electron temperature perturbation, as well as the measured variations in the VCR intensity, are not axisymmetric. Considering the second-order perturbation of the electron temperature, one can explain the violation of the axial symmetry in the images of axisymmetric beams. The difference in the VCR intensity profile along the $x$ and $y$ coordinates is due to the MM wave-induced spatial inhomogeneity of the electron heating by the DC electric field [29].

When a smooth and wide (i.e., wider than 2 cm) MMW beam affects the plasma slab, the influence of the electron heat conduction and other manifestations of nonlocality can be neglected in a first-order approximation. In this case, the perturbation in the electron temperature induced by a long pulse of MMW radiation with a sharp leading edge is given by [27]

$$\tilde{T}_e = \frac{2}{3} \frac{\gamma_0 W \tau_\varepsilon}{k N_{e0}} \left[ 1 - \exp\left(-(t-t_0)/\tau_\varepsilon\right) \right]. \tag{8}$$

The time history of the electron temperature perturbation, calculated using Eq. (8), coincides well with the measured time history of the VCR intensity variation. Therefore, the response time $\tau$ of the VC radiation is approximately equal to the characteristic time $\tau_\varepsilon$ of electron temperature variations due to the electron energy loss in electron-atom collisions.

# 5. Applications of the VCRD technique

The study of the performance and fundamentals of the VCRD technique, which was reviewed above, shows that this technique has some advantages over conventional techniques for MM imaging. In contrast to the imaging techniques, which use the receiving antenna arrays, a continuous medium with a small MMW reflection coefficient is exploited in the VCRD technique as an imager. Hence, it is possible to perform imaging of MMW beam profiles in the near-field region via the VCRD technique. The advantages of the VCRD technique over the thermographic techniques include a much higher energy sensitivity and a microsecond temporal resolution. These and some other advantages of the VCRD technique give hope for its applications for determination of the characteristics of output radiation from moderate-power MMW sources as well as for imaging and nondestructive testing with MM waves. At the same time, the VCRD technique has some peculiarities; therefore, experimental verification of the possibility of its use for solving applied problems is required. In this regard, Section 5 is focused on demonstration of two application capabilities of the VCRD technique. Subsection 5.1 discusses the experiments, where this technique is successfully used to measure the parameters of MM waves at the output of new-designed electron tubes. These studies are very relevant because short-wavelength millimeter waves are supposed to be widely used in new advanced radar, communication, diagnostic, and spectroscopy systems. However, in these frequency bands, the power of most types of modern CW and pulsed sources of EM waves is insufficient for use of thermographic imaging techniques. Due to its higher sensitivity, the VCRD technique can be successfully used for measuring the output characteristics of such MM wave sources. Subsection 5.2 provides an overview of experiments on the use of the VCRD technique for real-time imaging and nondestructive testing in the millimeter-wave band. Time-resolved imaging and NDT using MM waves are required for many applications [1–9]. Millimeter waves can penetrate through many opaque dielectric materials, such as paper, wood, fabric, ceramics, polymers, semiconductors, and others. This fact gives MMW imaging and NDT systems some advantage over optical and infrared systems, even though the spatial resolution of MMW systems is much worse than that of optical and IR systems. MMW imaging also has some advantages over THz imaging: first, atmospheric absorption and scattering is lower in the millimeter-wave region, and second, many types of conventional MMW sources and components are widely available. In contrast to EM radiation of the centimeter-wave band, which is also used for imaging and nondestructive testing, millimeter waves have a better spatial resolution. X-ray imaging also has some disadvantages compared to MMW imaging: first, the X-ray is ionizing and requires the implementation of stringent safety rules, and second, some materials, e.g., water, produce only low-contrast images in the X-ray region.

**5.1. Imaging of the beam profiles at the output of a D-band orotron and a W-band gyrotron**

Orotrons are vacuum electron sources of coherent EM radiation of the short-wavelength band of the MMW range. They are used in the microwave and NMR spectroscopy, for MMW frequency standards. A pulsed orotron OR-180 has been designed and manufactured by a collaboration of Russian organizations [46]. The orotron frequency was tuned electromechanically in the F and D bands. Output coupling of MMW radiation from the orotron cavity occurred through an oversized E-band rectangular waveguide. The design of the orotron assumes that the $TE_{10}$ mode of a rectangular waveguide will be excited predominantly in its output waveguide. Verification of this assumption and determination of the field profiles at the output of the orotron when it was tuned to the different frequencies were important steps towards the comprehension of the operating principle of this device and the improvement of its performance. For the solution of these problems, the VCRD technique for imaging of MM waves has been successfully used [30]. The scheme of this experiment is similar to that shown in Figure 3. Millimeter waves were generated by the orotron OR-180. The orotron pulse duration was 3 ms. A pyramidal horn antenna with aperture dimensions $14 \times 14$ mm$^2$ and 21 cm long was installed at the output of the E-band waveguide. The MMW electric field vector at the output of the horn was directed along the $y$ coordinate. The output of the horn was placed very close to the discharge tube window. Near-field intensity profiles at the output of a pyramidal horn antenna were imaged when the frequencies orotron radiation were 130, 140, and 150 GHz. The maximum orotron output power was about 0.3, 0.6, and 0.2 W for the frequencies 130, 140, and 150 GHz, respectively. Thin red lines in Figure 9 show the dependences of the VCR intensity variations on $x$ for $y' = 0$ and on $y$ for $x' = 0$, which were measured at the output of a horn antenna when the orotron frequency was 130 GHz (see Figures 9(a) and 9(b)) and 150 GHz (see Figures 9(c) and 9(d)). The VCR intensity profiles, which are shown in Figure 9, were averaged using 200 CCD camera frames recorded when MMW pulses were incident on the plasma. Figure 9 illustrates that the tuning the orotron frequency changes the intensity profile of the output MMW beam. In the frequency range 130–150 GHz in the E-band rectangular waveguide, besides the fundamental mode $TE_{10}^{\square}$, several higher modes can also be excited [43, 44]. By comparing the measured spatial distributions of VCR intensity variation with the profiles of the microwave-induced electron temperature perturbation, which were calculated using Eq. (7), it is possible to analyze the mode content of the orotron output radiation. Thick blue lines in Figures 9(a) and 9(b) show distributions of the first-order perturbation of the electron temperature on the coordinate $x$ for $y' = 0$ and on $y$ for $x' = 0$, respectively. These dependences were calculated assuming that in the orotron waveguide excited only one fundamental waveguide mode, $TE_{10}^{\square}$. For an orotron frequency of 130 GHz, the profiles of the VCR intensity are approximated well by these calculated distributions of the electron temperature perturbation. The measured relative value of the VCR intensity was higher than calculated electron temperature perturbation at the "tails" of distribution on $y$ for $x' = 0$ due to diffraction of the MM waves at the edges of a horn antenna, as well as the MM wave-induced nonuniformity of the electron heating by a DC electric field (see Section 4.2 and ref. [29]). Therefore, only fundamental waveguide mode is excited for an orotron radiation frequency of 130 GHz. The

same situation occurred when the orotron frequency was 140 GHz. For orotron frequencies of 130 GHz and 140 GHz, the admixture of higher modes does not exceed 10%. When the orotron was tuned to 150 GHz, multimode excitation of its output waveguide was observed. This is confirmed, particularly, by strong asymmetry of the distribution of the VCR intensity along the $y$ coordinate (see Figure 9(d)) and its broadening on $x$ (see Figure 9(c)). The results of the experiments on imaging of the MMW intensity profile for an orotron frequency of 150 GHz can be explained assuming that in the output waveguide, a $TE_{11}^{\square}$ mode is excited in addition to the fundamental mode $TE_{10}^{\square}$. Thick blue lines in Figures 9(c) and 9(d) show distributions of the first-order perturbation of the electron temperature on the $x$ coordinate for $y' = 0$ (see Figure 9(c)) and on $y$ for $x' = 0$ (see Figure 9(d)). The distributions were calculated assuming that the electric field amplitude ratio for the $TE_{10}^{\square}$ and $TE_{11}^{\square}$ modes is equal to $E^{TE 10}/E^{TE 11} = 3:2$ and the phase difference between them is $\pi/4$. Figures 9(c) and 9(d) show that good agreement between the results of calculation and the experimental data occurs for such an amplitude ratio and a phase difference for the two modes. At an orotron frequency of 150 GHz, the power of the spurious mode was about 40% of the power of the fundamental mode.
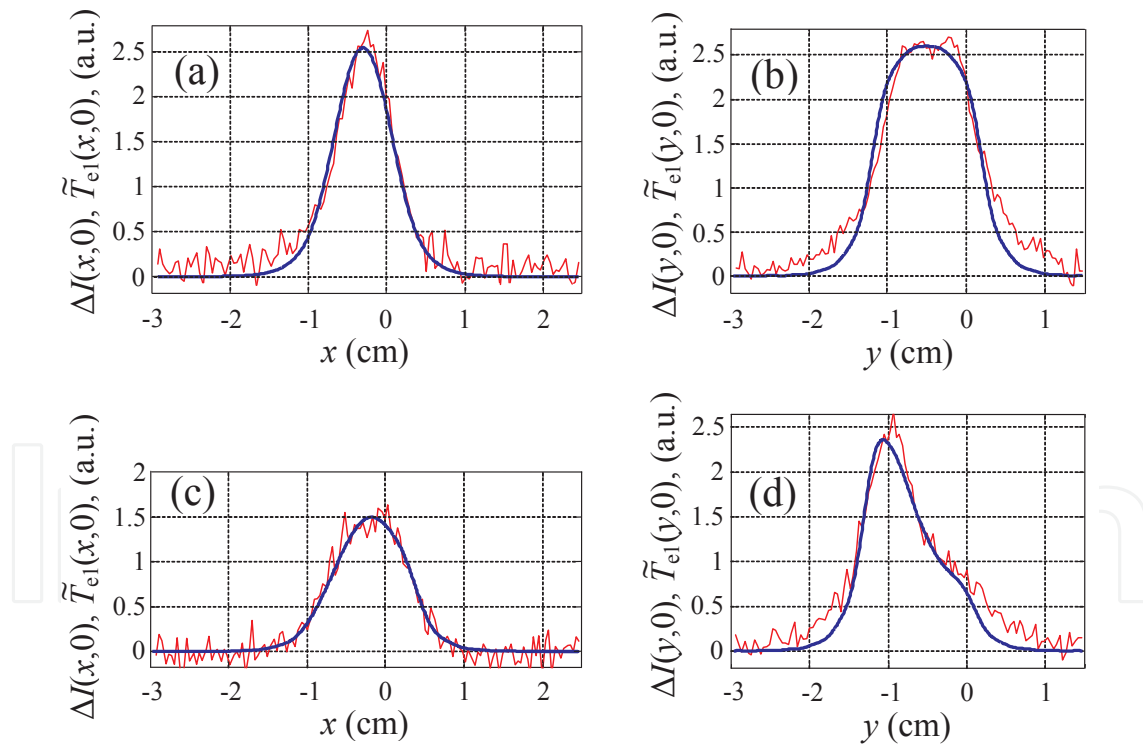


**Figure 9.** The dependences of the VCR intensity variations (thin red lines) on $x$ for $y' = 0$ ((a) and (c)) and on $y$ for $x' = 0$ ((b) and (d)), which were obtained at the orotron frequency 130 GHz ((a) and (b)) and 150 GHz ((c) and (d)). The first-order perturbation of the electron temperature (thick blue lines) vs. $x$ for $y' = 0$ ((a) and (c)) and vs. $y$ for $x' = 0$ ((c) and (d)).

The VCRD technique was applied for imaging of the field profiles at the output of a 110 GHz kilowatt-scale gyrotron with a pulsed magnetic field [32]. These experiments are of interest for

the improvement of this type of gyrotrons and for their successful exploitation in various applications. The scheme of this experiment is similar to that shown in Figure 3. The millimeter waves were output from the gyrotron cavity without mode conversion via a circular hollow metal waveguide 16 mm in diameter and about 200 mm long. A circular hollow metal waveguide 16 mm in diameter and 640 mm long was attached to the gyrotron waveguide. A conical horn antenna 140 mm long and having an aperture diameter of 40 mm was set at the output of the circular waveguide. The gyrotron power can be varied by changing the electron beam voltage and current. The pulse duration of the gyrotron was 60 μs. The CCD camera exposure time was 64 μs. The gyrotron was in the stage of debugging and improvements at the time of the experiments on imaging of its output field profiles. In accordance with the gyrotron design, its operating mode was the rotating mode $TE_{32}^O$ of a circular waveguide. In the first series of experiments, the length of the gyrotron cavity was by 1.5 times longer than optimal for its high-efficiency operation. The maximum output power of the gyrotron with that long cavity was about 3 kW. Figure 10(a) shows a 2D distribution of CVR intensity variation under the MMW effect, which was measured at the output of a conical horn for a gyrotron output power P = 1 kW. For such a power, the MMW intensity in the field maxima did not exceed the microwave breakdown threshold of the PC of a Cs-Xe discharge. The VCR image corresponds to the $TE_{32}^O$ mode pattern. The standing- wave pattern in the azimuthal direction occurred due to the presence of an admixture of the counter-rotating $TE_{32}^O$ mode. Figure 10(b) shows the image of VCR intensity variation recorded at the output of a horn antenna for the gyrotron power P = 3 kW. For such a power, the intensity of millimeter waves at their maxima exceeded the breakdown threshold of the plasma slab. Due to the strong increase of VCR intensity in the plasma breakdown areas, the image of the spatial distribution of the MMW intensity was distorted, i.e., it was much more contrasting than in reality. 2D distributions of the MMW intensity were calculated for different power ratios of the counter-rotating $TE_{32}^O$ modes of a circular waveguide. The best agreement between experimental data (Figure 10(a)) and computed distribution was obtained for a power of the spurious counter-rotating mode equal to about 0.5% of the power of the fundamental mode $TE_{32}^O$. Figure 10(c) shows the calculated 2D distribution of MMW intensity for $TE_{32}^O$ modes with such a power of the counter-rotating mode. The darker areas in Figure 10(c) correspond to the higher-intensity MM waves. In the second series of experiments, a new cavity was installed in the gyrotron. The length of this cavity was optimal for the high-efficiency gyrotron operation. As a result, the maximum gyrotron power increased up to about 10 kW. Figure 10(d) shows 2D distribution of the VCR intensity variation induced by MMW radiation from gyrotron with the optimal cavity. This pattern was recorded for reduced gyrotron power of about 1 kW. At such a gyrotron power, the MMW intensity did not exceed the breakdown threshold of the plasma. The image of MMW intensity profile (see Figure 10(d)) corresponds to the profile of the $TE_{32}^O$ mode, which rotates in one direction only. The admixture of the counter-rotating $TE_{32}^O$ mode at the output of the gyrotron with a new cavity was less than 0.1% in power.
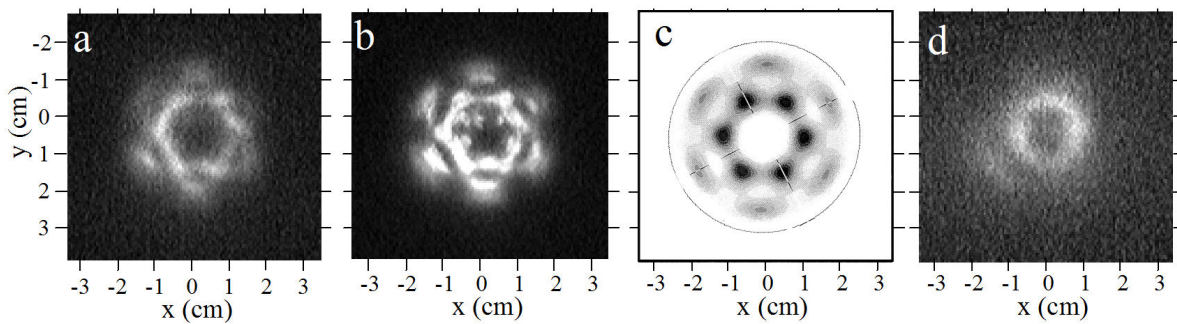
**Figure 10.** (a), (b), and (d) 2D distributions of the VCR intensity variation at the output of a 110 GHz gyrotron. (c) Calculated 2D distribution of MMW intensity for the $TE_{32}^{O}$ mode.

Thus, the VCRD technique has been successfully applied for determining of the fundamental waveguide modes of moderate-power MMW electron tubes and evaluating the relative power of some spurious modes.

### 5.2. Applications of the VCRD technique for imaging and nondestructive testing with MM waves

The VCRD technique has been used for active near-field MMW imaging and NDT via shadow projection method [33, 34]. In active-mode MMW imaging and NDT systems MM wave sources are used for object illumination [1–8]. A slab of the positive column of a Cs-Xe DC discharge has been used as a rapid imager for millimeter waves. In the near-field shadow projection method of MMW imaging, the objects are located close to the plasma imager. This is a drawback of the method in comparison with the quasioptical camera-mode method of MMW imaging, in which the object is located far away from the receiver [4, 6, 8, 13]. Realization of the active camera-mode method of imaging based on the VCRD technique is also feasible with using short-wavelength MM waves for object illumination. However, in the camera-mode method distortions of the images occur due to the diffraction and aberrations by lenses and mirrors. Diffraction and aberration effects are very significant when long-wavelength MM waves are used for object illumination. In this case, the use of the shadow projection method may provide a better image quality.

Figure 11 shows schematic of the experimental setup (top view), which was used for active near-field shadow projection MMW imaging using the VCRD technique [34]. A 35.4 GHz magnetron was used as a MMW source. The parameters of the magnetron were specified in Section 3. The MMW pulse length was about 10 ms. The repetition rate of MMW pulses was 12.5 Hz, i.e., half of the frame rate of the CCD camera. Camera frames, which were simultaneous with the MMW pulses, alternated with frames with the background VC radiation from the plasma slab. The CCD camera exposure time was 1 ms. The MMW beam was radiated by a pyramidal horn antenna with a length of 50 cm and aperture dimensions 6 × 8 cm². A plane-convex Teflon lens collimated the MMW beam. The polarization of the MMW beam was directed along the $x$ axis (see Figure 11). A test object was placed close to the window of the discharge tube. The width (FWHM) of the quasi-Gaussian beam in the object plane was about

8 cm. The MMW intensity in the center of the beam was approximately 0.3 W/cm². Time-averaged MMW intensity in the center of the beam was about 30 mW/cm². The MMW dose can be reduced by an order of magnitude by shortening the MMW pulse duration to the CCD camera exposure time. For this millimeter wave intensity, the MMW thermal effect on the majority of objects is not significant.[6] For the MMW intensity less than 1 W/cm², the VCR intensity $\Delta I(x, y)$ is directly proportional to the intensity of the MMW radiation incident on the plasma $W(x, y)$ (see Section 3); hence, the image of the VCR intensity variations corresponds to a 2D distribution of the MMW intensity behind the object. The effect of nonlocality of the MM wave-induced variation of the VCR intensity slightly blurs the MMW images.
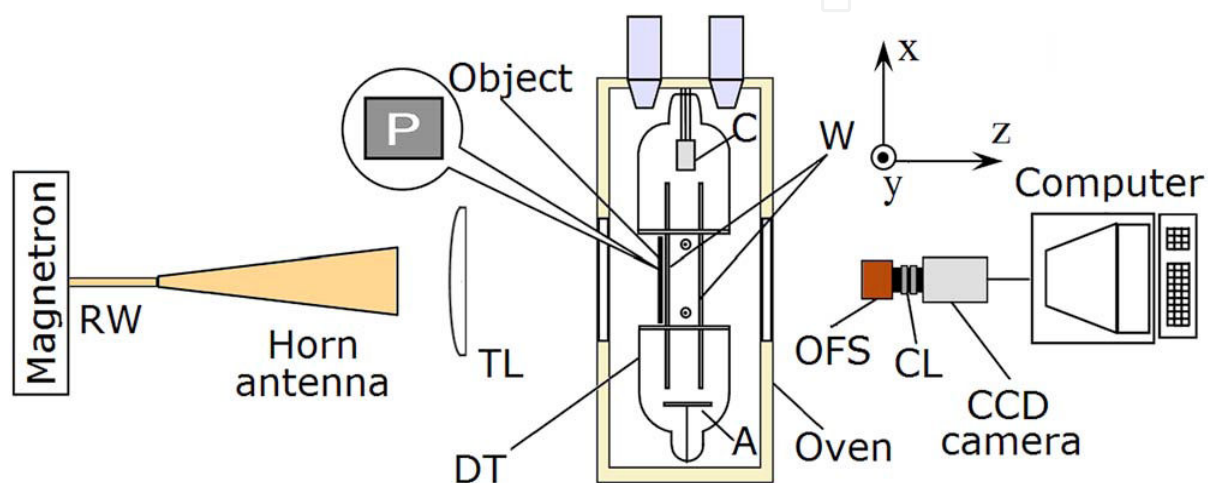


**Figure 11.** Schematic of the experimental setup (top view); RW: rectangular waveguide; TL: Teflon lens; DT: discharge tube; A: anode; C: cathode; W: quartz windows; OFS: optical filter set; CL: camera lens. Inset, front view of the test object placed before the tube window.

The near-field MMW images of the amplitude objects, which are made of materials that are opaque for MMWs, and the phase objects, which are transparent to the MMW radiation, have been obtained using the VCRD technique. At first, static amplitude and phase objects were imaged. The letters and numbers from IRMMW-THZ 08, an acronym for the name of the International conference, were used as the amplitude test objects. They were cut in the aluminum foil. The foils were glued on cardboard sheets. The letters and numbers were 50 mm high. The width of the rectangular strips transparent for MMWs was 12 mm. The images of the VCR intensity variation under the effect of the MM waves transmitted through the slit objects are shown in Figure 12. The single-shot signal-to-noise ratio for the images was about 20:1. The noise level of the images was given by the noise performance of the CCD camera. The obtained images were distorted by the diffraction because the plasma slab was located in the

6 The VCRD technique is well suited for inspection and MMW imaging of the inanimate objects. The time-averaged MMW intensity of 3mW/cm² is several times larger than the maximum MMW dose, which is permitted for general public use in the case of uniform MMW irradiation the whole human body [52]. However, this value is an order of magnitude less than the maximum permitted dose for local MMW irradiation of a part of the human body. Therefore, the VCRD technique cannot be used for entire-body personnel screening, but its applications for security screening and medical imaging with irradiation of a part of human body may be feasible.

Fresnel region. Nevertheless, all of the letters and numbers can easily be recognized. Figure 13(a) shows the image of letter E cut out of aluminum foil and glued on a cardboard sheet. The letter was 50 mm high and 45 mm wide. The width of the foil strips was 10 mm. The shape of this object, which is opaque for MM waves, can be easily determined from the image.
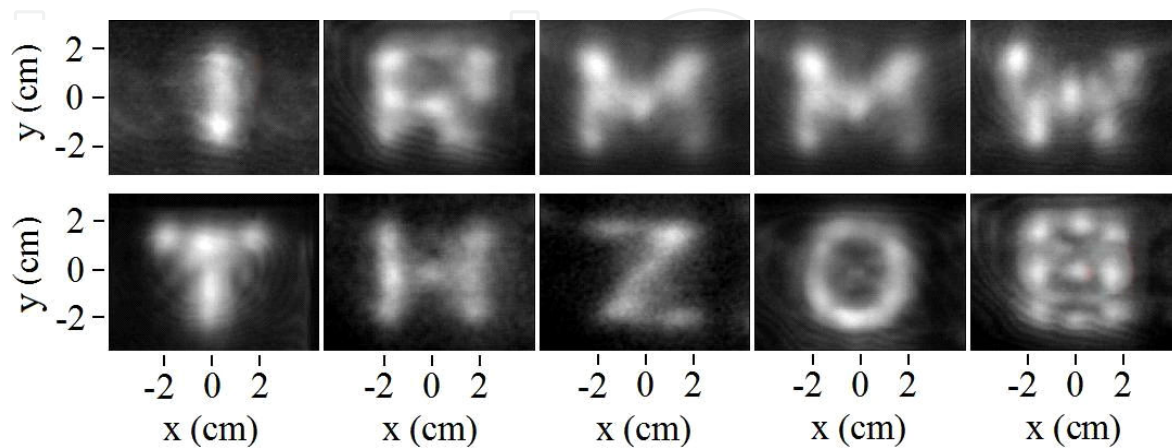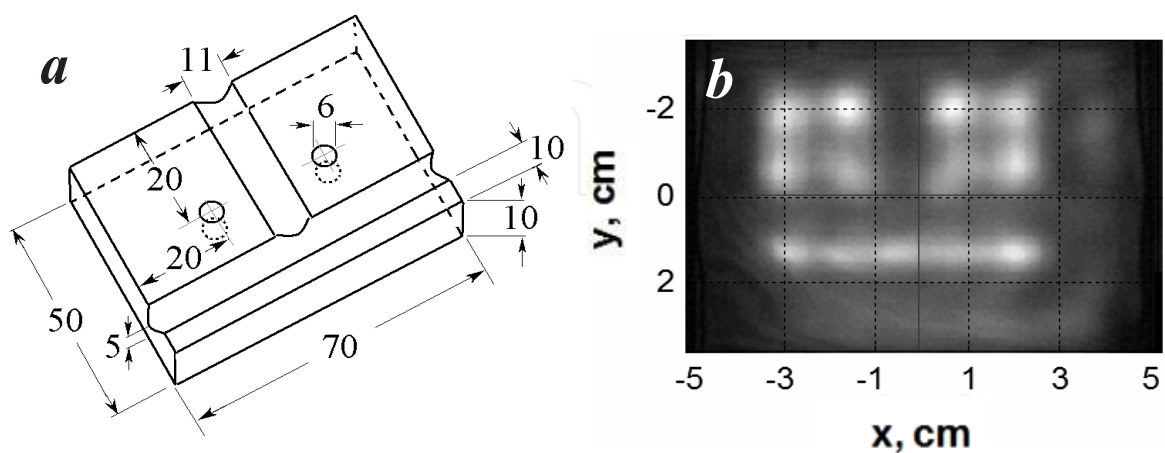


**Figure 12.** MMW transmission images of the letters and numbers from the acronym IRMMW-THZ 08 cut in aluminum foils.

Due to the peculiarities of the electromagnetic wave diffraction at the edge of transparent and opaque objects, the images of phase objects can have a higher quality as compared to the images of amplitude objects. The EM wave transmitted through a transparent dielectric slab with the thickness $L_C$ acquires an additional phase shift $\Delta\varphi_M = 2\pi\left(\sqrt{\varepsilon_M}-1\right)L_C/\lambda_M$, where $\varepsilon_M$ is the permittivity of the material from which the object is made, $\lambda_M$ is the wavelength of the MMW radiation. If the additional phase shift of the EM wave transmitted through the object differs from the multiple of $2\pi$, then the diffraction gives rise to a narrow minimum of the EM wave intensity in the near-field region behind the edge [53, 54]. The minimum is located between two maxima of intensity, i.e., an edge contrast enhancement occurs in the image of a phase object. Exploiting the VCRD technique, a shadow projection MMW image of a rectangular parallelepiped from Teflon ($\varepsilon_M \approx 2$) was obtained. The length, width, and thickness of the parallelepiped were 180, 28, and 6.8 mm, respectively. In the experiment, the long edges of the parallelepiped were directed parallel to the $y$ axis. When the MMW beam transmitted through Teflon parallelepiped, it acquired an additional phase shift which was equal to about $0.64\pi$. Figure 13(b) shows the 2D MMW image of the parallelepiped. Gray line in Figure 13(c) shows the dependence of the VCR intensity variation on $x$ for $y = 0$. The MMW intensity distribution in the near-field of the Teflon plate 28 mm width was calculated using the theory of Fresnel diffraction from a transparent thin plate [53, 54]. The black line in Figure 13(c) shows the dependence of the integral of the MMW intensity over the plasma slab thickness $W_S$ vs. the coordinate $x$ calculated for such a plate. Calculated dependence $W_S(x)$ is close to the experimental distribution of the VCR intensity variation. Images of more complex dielectric objects are shown in Figures 14 and 15. Figure 14(a) is a drawing of a rectangular Teflon plate with

two intersecting grooves having the form of half a cylinder. In the drawing, the dimensions are given in millimeters. Figure 14(b) shows the MMW image of this Teflon plate. The plate edges and both grooves are clearly seen in the image given in Figure 14(b). Perforating circular holes with a diameter of 6 mm are invisible. Figure 15(a) shows the MMW transmission image of a fish-shaped pumice-stone. The height, width, and thickness of the pumice-stone fish were 95, 58, and 18 mm, respectively. In the MMW images of the fish, as well as the Teflon plates, an edge contrast enhancement occurs. Figure 15(b) shows the MMW transmission image of three Septogal pellets (made by JADRAN, Croatia). The pellets were disks 16 mm in diameter and about 3.5 mm thick. The pellets were arranged as a trefoil and placed inside an envelope. Although the diameter of the pills is only twice the MMW wavelength, they are fairly well seen on the image. The experiments have demonstrated that the VCRD technique can be used for a real-time security screening, including the screening of drugs hidden in envelopes.
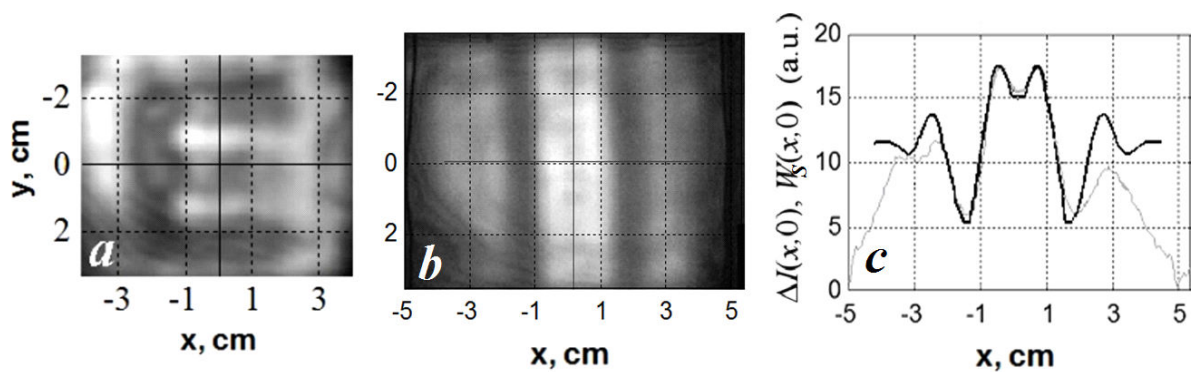


**Figure 13.** (a) MMW image of the letter E cut out of aluminum foil. (b) 2D MMW image of a rectangular parallelepiped from Teflon. (c) The dependences of the VCR intensity variation (gray line) and the MMW intensity integrated over the plasma slab thickness (black line) on $x$ for $y = 0$.



**Figure 14.** (a) A drawing of the rectangular plate with two intersecting grooves. (b) MMW transmission image of the Teflon plate.
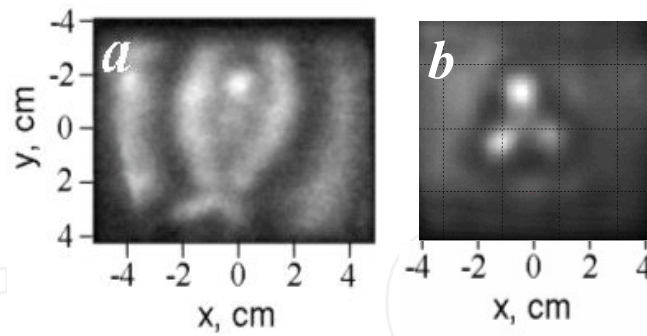
**Figure 15.** (a) MMW transmission image of a pumice-stone in the form of a fish. (b) MMW transmission image of three Septogal pellets.

The VCRD technique was used for time-resolved record of the MMW images of moving objects and registration of transient processes [34]. In particular, real-time shadow projection images of damped pendulum oscillation were obtained. The pendulum was a Teflon ring suspended by a thread about 15 cm long. The outer and inner ring diameters were 25 mm and 13 mm, respectively, and the ring was 8 mm thick. The ring affected the MMW beam as a three-zone phase filter which focused the MMW beam in the near field in a focal spot about 7 mm in diameter. The decay time of the pendulum oscillation was about 4 s, and the oscillation period was approximately 0.8 s. Figures 16(a) –16(e) show a sequence of MMW images of the pendulum motion, which was recorded at equal time intervals during half of the first period of pendulum oscillations. The process, by which a cylindrical glass tube filled with water became empty, was also imaged (see Figures 16(f) –16(j)). The inner and outer tube diameters were 6 and 8 mm, respectively. The tube filled with water was opaque for MMWs (see Figure 16(f)). After opening a valve which was located at the foot of the glass tube (outside the aperture), the water began to flow out of the tube. Figures 16(g) –16(i) show how the glass tube becomes transparent for MMWs as it is emptied. The water poured out of the tube for about 1 s. The MMW transmission image of the empty tube is shown in Figure 16(j). The tube wall is well defined in Figure 16(j) because of the considerable difference in the refractive indices of glass and air.
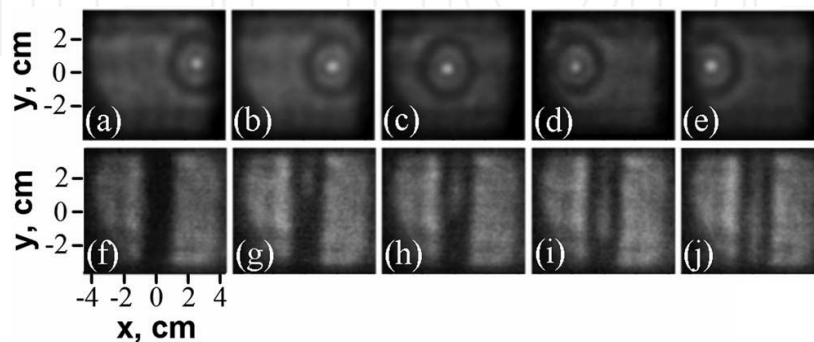


**Figure 16.** (a)–(e) Real-time MMW transmission images of pendulum motion obtained during one-half of the oscillation period. (f)–(j) MMW transmission movie showing how a glass tube filled with water was emptied.

## 6. Conclusions

The chapter presents a review of the VCRD technique for imaging and measurement of the 2D spatial profiles of MMW intensity based on the use of visible continuum radiation from the positive column of a Cs-Xe DC discharge. The design of the discharge tube and the experimental setup that were used to create a CW homogeneous slab of thermal nonequilibrium discharge in a mixture of medium pressure xenon and cesium vapor were described. Results of the study of the basic parameters of the positive column of a Cs-Xe discharge were presented. Three modes of the positive column of a Cs-Xe discharge were observed depending on the tube temperature for a fixed value of the discharge current: a constricted PC, a spatially homogeneous PC, and a PC with a filament. For imaging of MM waves, a wide homogeneous PC plasma slab was used. The MMW effects on the plasma slab have been experimentally studied. It was shown that brightness of the VC radiation from the PC plasma increases by several times when the MMW intensity changes from zero to the threshold of the microwave-induced plasma breakdown. The model experiments on imaging of the field patterns of horn antennas and quasioptical beams have been performed using the VCRD technique. These experiments demonstrate that the VCRD technique can be used for a good-quality time-resolved imaging of MMW beams with a width of about 10 mm or more. The temporal resolution of the technique is about 0.8 μs. It was shown that the VCRD technique is wideband and can be used for imaging of the intensity profiles of the EM waves in the entire MMW band. Energy flux sensitivities of about 10 μJ/cm² in the Ka band and about 200 μJ/cm² in the D band have been demonstrated.

The fundamentals of the VCRD technique for imaging of MMWs have been discussed. The studies of the nature of the visible continuum radiation from the PC of a Cs-Xe discharge and mechanism of microwave-induced variations in the VCR intensity were reviewed. It is shown that the electron-xenon atom bremsstrahlung is the dominant component of the visible continuum emitted by the homogeneous PC of a Cs-Xe discharge. The increase in the e-Xe bremsstrahlung intensity in the visible region is caused by an increase in the number density of electrons with the energy more than 2 eV, which is a result of the additional electron heating induced by the MM waves. The profiles of the microwave-induced variation in the intensity of the VC radiation from the plasma slab were analytically modeled. It was proved that the nonlocality of the microwave-induced variations in the VC radiation intensity, as well as the spatial resolution of the VCRD technique of MMW imaging, are primarily determined by the influence of the electron heat conduction. The line spread function for the VCRD technique has been calculated. It was found that its width is about 2 mm. It was shown that the main cause of the axial asymmetry of images of the axisymmetric MMW beams is the MM wave-induced spatial inhomogeneity of the electron heating by a DC electric field.

The final part of the paper reviews some applications of the CVRD technique for MMW imaging. The experiments on imaging of the output field pattern of a D-band watt-scale orotron and a W-band kilowatt-scale gyrotron were described. Operating modes for these vacuum tubes were identified and the power of spurious modes were determined. Applications of the VCRD technique for real-time imaging and nondestructive testing using MM waves are also

the subject of the final part of the review. Near-field shadow projection images of the objects which are opaque and transparent for MM waves have been obtained using pulsed watt-scale MM waves for object illumination. Near video frame rate millimeter-wave shadowgraphy has been demonstrated. It was shown that this technique can be used for a single-shot security screening, including the screening of drugs hidden in envelopes, and for a real-time imaging of the transient processes.

## Acknowledgements

## Author details

Mikhail S. Gitlin[*]

Address all correspondence to: gitlin@appl.sci-nnov.ru

Institute of Applied Physics, Russian Academy of Sciences, Nizhny Novgorod, Russia

## References

[1] Bolomey J.-C. Recent European developments in active microwave imaging for industrial, scientific, and medical applications. IEEE Trans. Microwave Theory Tech. 1989;37:2109–2117. DOI: 10.1109/22.44129

[2] Kharkovsky S., Zoughi R. Microwave and millimeter wave nondestructive testing and evaluation—Overview and recent advances. IEEE Instrum. Meas. Mag. 2007;10:26–38. DOI: 10.1109/MIM.2007.364985

[3] Gomez-Maqueda I., Almorox-Gonzalez P., Callejero-Andres C., Burgos-Garcia M. A millimeter-wave imager using an illuminating source. IEEE Microwave Mag. 2013;14:132–138. DOI: 10.1109/MMM.2013.2248652

[4] Sato M., Mizuno K. Millimeter-wave imaging sensor. In: Minin I, editor. Microwave and Millimeter Wave Technologies from Photonic Bandgap Devices to Antenna and Applications. InTech; 2010. p. 331–349. ISBN: 978-953-7619-66-4

[5]   Ahmed S. S., Schiessl A., Gumbmann F. F., Tiebout M., Methfessel S., Schmidt L.-P. Advanced microwave imaging. IEEE Microwave Mag. 2012;13:26–43. DOI: 10.1109/MMM.2012.2205772

[6]   Tang A., Gu Q. J., Chang M.-C. F. CMOS receivers for active and passive mm-wave imaging. IEEE Communications Magazine. 2011;49:190–198. DOI: 10.1109/MCOM.2011.6035835

[7]   Sheen D. M., McMakin D. L., Hall T. E. Three-dimensional millimeter-wave imaging for concealed weapon detection. IEEE Trans. Microwave Theory Tech. 2001;49:1581–1592. DOI: 10.1109/22.942570

[8]   Watabe K., Shimizu K., Yoneyama M., Mizuno K. Millimeter-wave active imaging using neural networks for signal processing. IEEE Trans. Microwave Theory Tech. 2003;51:1512–1515. DOI: 10.1109/TMTT.2003.810132

[9]   Greeney N. S., Scales J. A. Dielectric microscopy with submillimeter resolution. Appl. Phys. Lett. 2007;91:222909. DOI: 10.1063/1.2818674

[10]  Ozhegov R., Gorshkov K., Vachtomin Y., Smirnov K., Finkel M., Goltsman G., Kiselev O., Kinev N., Filippenko L., Koshelets V. Terahertz imaging system based on superconducting heterodyne integrated receiver. In: Corsi C., Sizov F, editors. THz and Security Applications, Detectors, Sources and Associated Electronics for THz Applications. Netherlands: Springer; 2014. p. 113-125. DOI: 10.1007/978-94-017-8828-1_6

[11]  Kopeika N. S., Fartiat N. H. Video detection of millimeter waves with glow-discharge tubes. IEEE Trans. on Electron Devices. 1975;22:534–548. DOI: 10.1109/T-ED.1975.18175

[12]  Abramovich A., Kopeika N. S., Rozban D. Design of inexpensive diffraction limited focal plane arrays for millimeter wavelength and terahertz radiation using glow discharge detector pixels. J. Appl. Phys. 2008;104:033302-1-033302-4. DOI: 10.1063/1.2963714

[13]  Brooker G., Johnson D. G. Low-cost millimeter wave imaging using a commercial plasma display. IEEE Sensors J. 2015;15:3557-3564. DOI: 10.1109/JSEN.2015.2393306

[14]  Hisatake S., Nguyen Pham H. H., Nagatsuma T. Visualization of the spatial-temporal evolution of continuous electromagnetic waves in the terahertz range based on photonics technology. Optica. 2014;1:365–371. DOI: 10.1364/OPTICA.1.000365

[15]  Tsuchiya M., Kanno A., Sasagawa K., Shiozawa T. Image and/or movie analyses of 100-GHz traveling waves on the basis of real-time observation with a live electrooptic imaging camera. IEEE Trans. Microwave Theory Tech. 2009;57:3373-3379. DOI: 10.1109/TMTT.2009.2033890

[16]  Bazhulin A. P., Vinogradov E. A., Irisova N. A., Fridman S. A. Obtaining a visible image of radio emission in the millimeter band. JETP Lett. 1968;8:160–162.

[17] Cherkassky V. S., Gerasimov V. V., Ivanov G. M., Knyazev B. A., Kulipanov G. N., Lukyanchikov L. A., Merzhievsky L. A., Vinokurov N. A. Techniques for introscopy of condense matter in terahertz spectral region. Nuclear Instruments and Methods in Physics Research A. 2007;575:63–67. DOI: 10.1016/j.nima.2007.01.025

[18] Chang T. H., Yu C. F., Fan C. T. Polarization-controllable TE21 mode converter. Rev. Sci. Insrum. 2005;76:074703-1-074703-6. DOI: 10.1063/1.1942528

[19] Junchang L., Yanmei W. An indirect algorithm of Fresnel diffraction. Optics Communications. 2009;282:455–458. DOI: j.optcom.2008.10.060

[20] Thumm M. K., Kasparek W. Passive high-power microwave components. IEEE Trans. on Plasma Science. 2002;30:755–786. DOI: 10.1109/TPS.2002.801653

[21] Malygin V. I., Paveljev A. V. Determination of the mode content in spurious microwave radiation of the gyrotron with a straight axisymmetric output. Int. J. Infrared Millimeter Waves. 1999;20:33–56. DOI: 10.1023/A:1021747516720

[22] Jawla S., Hogge J-P., Alberti S., Goodman T., Piosczyk B., Rzesnicki T. Infrared measurements of the RF output of 170-GHz/2-MW coaxial cavity gyrotron and its phase retrieval analysis. IEEE Trans. on Plasma Sci. 2009;37:414-424. DOI: 10.1109/TPS. 2008.2011488

[23] Idehara T., Kosuga T., Agusu L., Ogawa I., Takahashi H., Smith M. E., Dupree R. Gyrotron FU CW VII for 300 MHz and 600 MHz DNP-NMR spectroscopy. J. Infrared Millim. Terahz Waves. 2010;31:763–774. DOI: 10.1007/s10762-010-9637-9

[24] Gold S. H., Fliflet A. W., Manheimer W. M., McCowan R. B., Lee R. C., Granatstein V. L., Hardesty D. L., Kinkead A. K., Sucy M. High peak power Ka-band gyrotron oscillator experiments with slotted and unslotted cavities. IEEE Trans. on Plasma Sci. 1988;16:142–148. DOI: 10.1109/27.3806

[25] Bratman V. L., Denisov G. G., Ofitserov M. M., Korovin S. D., Polevin S. D., Rostov V. V. Millimeter-wave HF relativistic electron oscillators. IEEE Trans. on Plasma Sci. 1987;15:2–15. DOI: 10.1109/TPS.1987.4316655

[26] Cook A., Shapiro M., Temkin R. Pressure dependence of plasma structure in microwave gas breakdown at 110 GHz. Appl. Phys. Letters. 2010;97:11504-1-011504-3. DOI: 10.1063/1.3462320

[27] Gitlin M. S., Golovanov V. V., Spivakov A. G., Tsvetkov A. I., Zelenogorskiy V. V. Time-resolved imaging of millimeter waves using visible continuum from the positive column of a Cs-Xe DC discharge. J. Appl. Phys. 2010;107:063301-1-063301-11. DOI: 10.1063/1.3327218

[28] Gitlin M. S., Spivakov A. G. Mechanism of the electric field effect on the intensity of visible continuum emission from the positive column of gas discharge in a cesium vapor-xenon mixture. Tech. Phys. Lett. 2007;33:205-208. DOI: 10.1134/ S1063785007030078

[29] Gitlin M. S., Fedotov A. E., Stukachev S. E., Tsvetkov A. I. Nonlocality of microwave-induced variations in the intensity of the visible continuum from a medium-pressure cesium-xenon dc discharge. Physics of Plasmas. 2012;19:033508-1-033508-11. DOI: 10.1063/1.3692077

[30] Fedotov A. E., Gitlin M. S., Golovanov V. V., Perminov A. O., Stukachev S. E. Imaging of short millimeter waves using the visible continuum emitted by the Cs-Xe DC discharge. In: Proc. Sixth Int. Kharkov Symposium on Physics and Engineering of Microwaves, Millimeter and Submillimeter Waves and Workshop on Terahertz Technologies; Kharkov. Kharkov, Ukraine: IRE NASU; 2007. 263–265.

[31] Gitlin M. S., Zelenogorsky V. V., Perminov A. O. Microwave beam imaging by recombination continuum from the positive column of gas discharge in a cesium vapor–xenon mixture. Tech. Phys. Letters. 2002;28:445–447. DOI: 10.1134/1.1490955

[32] Gitlin M. S., Glyavin M. Yu., Luchinin A. G., Zelenogorsky V. V. Imaging the output field pattern of a 110 GHz gyrotron with pulsed magnetic field using recombination continuum emitted by a slab of the Cs-Xe DC discharge. IEEE Trans. on Plasma Science. 2005;33:380-381. DOI: 10.1109/TPS.2005.845294

[33] Gitlin M. S., Golovanov V. V., Tsvetkov A. I. Real-time shadow projection millimeter-wave imaging using visible continuum from a slab of the Cs-Xe DC discharge. IEEE Trans. on Plasma Sci. 2008;36:1398–1399. DOI: 10.1109/TPS.2008.920901

[34] Gitlin M. S., Tsvetkov A. I. Real-time millimeter-wave shadowgraphy using the visible continuum from a slab of the Cs-Xe DC discharge. Appl. Phys. Lett. 2009;94:234102-1-234102-3. DOI: 10.1063/1.3152285

[35] Gitlin M. S., Epstein I. L., Lebedev Yu. A. Modeling of the positive column of a medium pressure Cs-Xe dc discharge affected by a millimeter wave pulse. J. Phys. D: Appl. Phys. 2013;46:415208-1-415208-11. DOI: 10.1088/0022-3727/46/41/415208

[36] Bogatov N. A., Gitlin M. S., Dikan D. A., Luchinin G. A. Cs-Xe dc gas discharge as a fast highly nonlinear volumetric medium for microwaves. Phys. Rev. Lett. 1997;79:2819–2822. DOI: 10.1103/PhysRevLett.79.2819

[37] Wazink J. H., Polman J. Cesium depletion in the positive column of Cs-Ar discharge. J. Appl. Phys. 1969;40:2403–2408. DOI: 10.1063/1.1658005

[38] van Tongeren H. Positive column of the Cs-Ar law-pressure discharge. J. Appl. Phys. 1974;45:89–96. DOI: 10.1063/1.1663024

[39] Batenin V. M., Chinnov V. F. Electron bremsstrahlung in the field of argon or helium atoms. Sov. Phys. JETP. 1972;34:30–33.

[40] Golubovskii Yu. B., Kagan Yu. M., Komarova L. L. Diagnostics of the discharge in argon at medium pressures by bremsstrahlung continuum. Opt. Spectrosc. (USSR). 1972;33:646–648.

[41] Park J., Henins I., Herrmann H. W., Selwyn G. S. Neutral bremsstrahlung measurement in an atmospheric-pressure radio frequency discharge. Phys. Plasmas. 2000;7:3141–3144. DOI: S1070-664X(00)03808-8

[42] Raizer Y. P. Gas Discharge Physics. Berlin: Springer-Verlag; 1991. 449 p.

[43] Harvey A. F. Microwave Engineering. London and New York: Academic Press; 1963. 1313 p.

[44] Marcuvitz N. Waveguide Handbook. London: P. Peregrinus; 1986. 434 p.

[45] Camparo J., Fathi G. Effects of rf power on electron density and temperature, neutral temperature, and Te fluctuations in an inductively coupled plasma. J. Appl. Phys. 2009;105: 103302-1-103302-9. DOI: 10.1063/1.3126488

[46] Bratman V. L., Dumesh B. S., Fedotov A. E., Makhalov P. B., Movshevich B. Z., Rusin F. S. Terahertz orotrons and oromultipliers. IEEE Trans. Plasma Sci. 2010;38:1466–1471. DOI: 10.1109/TPS.2010.2041367

[47] Clarricoats P. J. B., Olver A. D. Corrugated horns for microwave antennas. London: P. Peregrinus; 1984. 231 p.

[48] Rutscher A., Pfau S. On the origin of visible continuum radiation in rare gas glow discharges. Physica C. 1976;81:395–402. DOI: 10.1016/0378-4363(76)90078-4

[49] de Regt J. M., van Dijk J., van der Mullen J. A. M., Schram D. C. Components of continuum radiation in an inductively coupled plasma. J. Phys. D: Appl. Phys. 1995;28:40–46. DOI: 10.1088/0022-3727/28/1/008

[50] Burm K. T. A. L. Continuum radiation in a high pressure argon–mercury lamp. Plasma Sources Sci. Technol. 2004;13:387–394. DOI: 10.1088/0963-0252/13/3/004

[51] Agnew L., Reichelt W. H. Identification of the ionic species in a cesium plasma diode. J. Appl. Phys. 1968;39:3149–3155. DOI: 10.1063/1.1656749

[52] Wu T., Rappaport T. S., Collins C. M. Safe for generations to come. IEEE Microwave Mag. 2015;16:65–84. DOI: 10.1109/MMM.2014.2377587

[53] Anokhov S. P. Plane wave diffraction by a perfectly transparent half-plane. J. Opt. Soc. Am. A. 2007;24:2493–2498. DOI: 10.1364/JOSAA.24.002493

[54] Amiri M., Tavassoly M. T. Fresnel diffraction from 1D and 2D phase steps in reflection and transmission modes. Optics Communications. 2007;272:349–361. DOI: 10.1016/j.optcom.2006.11.048